 ©2012 Uspekhi Fizicheskikh Nauk, Russian Academy of Sciences

INSTRUMENTS AND METHODS OF INVESTIGATION

PACS numbers: **41.50.+h**, **42.79.–e**, 95.55.Ka

Precision imaging multilayer optics for soft X-rays and extreme ultraviolet bands

M M Barysheva, A E Pestov, N N Salashchenko, M N Toropov, N I Chkhalo

DOI: 10.3367/UFNe.0182.201207c.0727

Contents

1. Introduction 681
2. Imaging optical elements for soft X-ray and extreme ultraviolet radiations 682
3. Multilayer interference structures for soft X-ray and extreme ultraviolet radiations 683
4. Methods for investigation and precision correction of the shape of optical elements with supersmooth surfaces 687
5. Applications of ultrahigh-precision X-ray optics 691
5.1. Projection nanolithography; 5.2 X-ray microscopy; 5.3 X-ray astronomy; 5.4 Superhigh soft X-ray fields
6. Conclusion 698
References 698

Abstract. **Optical methods that provide high diffraction image quality with a spatial resolution of several to tens of nanometers and are in demand in such areas as projection lithography, X-ray microscopy, astrophysics, and fundamental research on the interaction of matter (vacuum) with ultrahigh (10^{20} – 10^{23} W cm^{-2}) electromagnetic fields are reviewed in terms of fabrication and testing technologies and possible use in the 2 – 60 nm wavelength range. The current worldwide status of and recent achievements by the Institute for Physics of Microstructures of the Russian Academy of Sciences (RAS) in the field are discussed.**

1. Introduction

The tasks of microscopy for objects of different natures and the fabrication of microstructures by photolithographic techniques are solved, as a rule, with the employment of radiation in the $\lambda \approx 200-600$ nm spectral range. The key parameter which characterizes the entire class of devices employed in this case is spatial resolution, which is limited by light diffraction at the output aperture of the optical system. According to the Rayleigh criterion, the diffraction resolution limit $\delta x = k\lambda/\mathrm{NA}$ of an optical system is defined by the wavelength λ and the lens numerical aperture NA ($\mathrm{NA} = n \sin\alpha$, where n is the refractive index of the medium between the lens and the image plane, and α is half of the output angular aperture of the lens). The proportionality coefficient k is determined by the coherence properties of light and the mode of object illumination, and varies between 0.25 and 0.77; for incoherent irradiation, one has $k = 0.61$. Therefore, the resolution of optical systems amounts to about one half of the wavelength, or worse than 100 nm. This limitation has come into sharp conflict with the trend of recent decades towards mastering the nanoworld (characteristic geometrical dimensions below 100 nm); in particular, this jeopardized at one time the applicability of Moore's law — the doubling of electronic component (transistor) density on a chip every year and a half [1].

In the area of microcircuit fabrication (photolithography), this lent impetus to the search for alternative ways of composing microstructures, for instance, with the aid of probe microscopes [2]. Great hopes were and are still pinned on multibeam [3] and projection [4] electron and ion lithographies [5], and on nanoprinting technology [6]. All these methods have found their niches and continue to develop. Nevertheless, traditional photolithography has proved to be beyond comparison for the mass production of microcircuits. This was made possible by the wide application of so-called resolution enhancement techniques [7]. Of these, mention should be made of purely optical ones, which decrease the k coefficient (for instance, by using oblique illumination and optimizing the coherent properties of the light incident on a mask), as well as the employment of correcting, phase-shifting, or absorbing layers on the mask. The involvement of an immersion liquid made it possible to improve the resolution by almost one and a half times. The potentials of immersion have not been exhausted, and the search for new liquids with a higher refractive index is being continued. Among the nonoptical methods of enhancing the resolution are technologies that harness the physicochemical photoresist properties and step-by-step topological pattern formation, when, e.g., elements are formed through a period (double patterning technology) [8].

M M Barysheva, A E Pestov, N N Salashchenko, M N Toropov, N I Chkhalo Institute for Physics of Microstructures, Russian Academy of Sciences,
ul. Ul'yanova 46, 603950 Nizhny Novgorod, Russian Federation
Tel. +7 (831) 438 56 03
Fax +7 (831) 438 55 55
E-mail: chkhalo@ipm.sci-nnov.ru

Received 27 June 2011
Uspekhi Fizicheskikh Nauk **182** (7) 727 – 747 (2012)
DOI:10.3367/UFNr.0182.201207c.0727
Translated by E N Ragozin; edited by A Radzig

At a photoresist exposure (writing) wavelength of 193 nm, modern lithographic facilities (scanners) and standard technological procedures already provide a resolution of 32 nm [9], and up to 22 nm in laboratories [10]. The almost fivefold 'overcoming' of the diffraction resolution limit is due to the enhanced complexity and corresponding rise in the cost of the equipment and the chip production technology. In lieu of the simplest topology formation procedure, which comprises resist deposition on a plate, exposure, and development, dozens of new operations emerge.

While attempts in lithography to substantially advance into the nanometer resolution domain somehow do meet with success, of all the methods of improving resolution in microscopy only immersion works practically. The potentialities of classical microscopy in attaining the ultimate spatial resolution have been virtually exhausted. An alternative is provided by optical near-field microscopy, which permits attaining a resolution at a level of tens of nanometers [11]. As in the case of lithography, however, the price to be paid for this improvement is complex scanning systems and several functional limitations.

Reaching nanometer-scale resolution in classical microscopy and photolithography schemes is possible if use is made of shorter wavelengths, $\lambda < 100$ nm, i.e. the domain of extreme ultraviolet (EUV) and soft X-ray (SXR) radiations. The efficiency of this approach was demonstrated by research in the area of projection EUV lithography at a wavelength of 13.5 nm. Even at the first experimental lithography facilities it was possible to achieve diffraction-limited spatial resolution, which was as good at that time as the resolution of more sophisticated lithographic facilities operating at a wavelength of 193 nm [12, 13]. In recent years, a new wavelength, $\lambda \approx 6.7$ nm, is actively being discussed for application in next-generation lithography [14, 15].

Along with the prospect of improving the spatial resolution, the SXR and EUV ranges ($\lambda \sim 1-60$ nm) for several reasons are of major interest for experimental physics, astronomy, chemistry, and microbiology. First, the energy levels of the majority of atoms lie in this spectral domain, which underlies the resonance nature of radiation–matter interaction and thereby gives researchers unique and reliable information about the internal structure of atoms and their interaction with the nearest neighbors [16]. Second, this range contains the intrinsic radiation peaks of laboratory plasmas and the line radiation of the main impurity ions, making X-ray spectroscopy very convenient for plasma diagnostics [17]. The line radiation of the solar corona is one of the most reliable sources of information about the physical processes occurring in the Sun [18]. Third, the weak scattering of the radiation and its relatively large penetration depth in substances permit carrying out tomographic investigations of 'thick' subjects. In combination with nanometer resolution, this opens up new avenues for physical investigations of condensed matter, as well as for chemistry and microbiology. Fourth, the weak absorption of radiation with energy below the ionization potential of the qth atomic level, $E_{\rm ph} < E_{{\rm i}q}$, and a sharp absorption jump on exceeding the electron binding energy underlie, in many cases, so high a contrast of absorption images (for instance, of proteins in an aqueous medium) that obtaining a quality object image requires an irradiation dose several orders of magnitude lower than that required with the use of 'nonresonance' X-ray radiation or fast electrons [19]. This is of fundamental importance in some cases, because it permits studying 'living' biological specimens with a resolution of tens of nanometers or organic objects ranging from several to tens of nanometers in size, which are placed in a 'thick' (> 1 μm) matrix, for instance, in an aqueous suspension.

The combination of the capabilities of X-ray techniques for the study of substances (diffractometry, X-ray and photoelectron spectroscopies, small-angle scattering, etc.) with the attainment of nanometer spatial resolution opens unique possibilities for the nanophysics of condensed matter [16, 20, 21]. In particular, mention should be made of pioneering work in nanomagnetism, where it was possible to observe domain formation in magnetic films with a spatial resolution of 15 nm using the effect of magnetic dichroism [20].

The main components of any optical instrument, which determine its characteristics, are radiation sources, monochromators, imaging systems, and radiation detectors. Recent years have seen the development of a number of accelerator-based sources (synchrotrons [22], free-electron lasers [23]) of EUV and SXR radiation, which exhibit the energy, spatio-angular, polarization, and coherent characteristics of radiation beams satisfying the present-day — and in some cases future — requirements of the physics of radiation–matter interaction. The concurrent development of high-power laboratory radiation sources (high-current gas discharges [24], plasmas produced by laser irradiation of a substance with an intensity of $10^{11}-10^{13}$ W cm^{-2} [25], and X-ray lasers [26, 27]) and the fabrication of efficient polarizers and phase-shifting elements based on multilayer interference structures [28, 29] have provided a realistic opportunity to solve a broad spectrum of problems in laboratory conditions, which had earlier been solved only in the synchrotron centers.

A serious limitation, which until recently had retarded the possible advantageous application of the short wavelengths of EUV and SXR radiations for achieving nanometer spatial resolution, was the absence of large-aperture precision optics with the capability of realizing diffraction quality resolution imaging.

Our work reviews modern approaches to X-ray imaging and discusses the specific character of applying these techniques in the SXR and EUV ranges. We analyze the prospects of and the main problems encountered in the fabrication, metrology, and employment of precision SXR/EUV optics in scientific and technological investigations. Much consideration is being given to short-period multilayer mirrors which form the basis for this optics, as well as to the methods of studying the irregularities of supersmooth surfaces of the substrates for multilayer mirrors throughout the spectral range of spatial frequencies which determine imaging with subnanometer precision. The latest advances in this area are reported. Along with obvious applications to lithography and microscopy, attention is given to new capabilities of precision X-ray optics for surface diagnostics with nanometer spatial resolution and the production of superstrong magnetic fields.

2. Imaging optical elements for soft X-ray and extreme ultraviolet radiations

The problems encountered in developing optics for the SXR and EUV radiations arise from the special character of radiation–matter interaction in these ranges, namely from a close-to-unity refractive index $|n-1| \ll 1$ and a strong radiation absorption in virtually all materials (the absorp-

tion lengths vary from hundredths of to several micrometers) [30, 31]. Owing to the low refraction, as well as to the fact that the refractive index is smaller than unity in the majority of cases, appreciable reflection is observed only at small grazing angles of incidence, $\theta < \theta_c \approx 2\lambda$, where θ_c is the critical angle of total external reflection, with the angles expressed in degrees, and the wavelengths in nanometers [32]. To construct images in the SXR and EUV ranges, advantage is therefore taken of grazing incidence optics (single mirrors, Kirkpatrick–Baez [33] and Wolter [34] systems), which possesses a small numerical aperture and large geometrical aberrations and, as a consequence, a low spatial resolution. Mention should nevertheless be made of Ref. [35], where a one-dimensional X-ray beam focusing at the SPring-8 synchrotron produced a spot with a presently record width of 7 nm with precisely the aid of a grazing incidence mirror. However, these were small-aperture cylindrical mirrors suitable only in the hard X-ray range ($\lambda \sim 0.1$ nm).

To collect and form X-ray beams, use is also made of capillary optics; however, it suffers from the same drawbacks as grazing incidence mirrors and the resolution achieved to date does not exceed several micrometers [36]. Beryllium-based waveguide structures exhibit a somewhat better resolution [37], but they are characterized by a low light-gathering power and provide a submicron beam only in one direction and in the immediate proximity (several micrometers) to the waveguide end, which severely hinders their employment in experiments.

In recent years, the technology of refractive X-ray lenses has been making rapid strides. The focal distance F of a lens made of a material with a refractive index n and with one refracting surface of radius R is $F = R/(n-1)$. For clarity, we give a numerical estimate of the parameters of a silicon lens with a focal distance $F = 1$ m at a wavelength $\lambda = 1$ nm. The real part of the refractive index $n = 0.99972$ [31], the radius of curvature $R = -282$ μm, and the absorption length is 4.85 μm [31]. Therefore, while focusing lenses of the optical range are convex in shape, in the X-ray range they are concave. To obtain a reasonable focal length, the radius of surface curvature must be as short as tens or hundreds of micrometers, depending on the working wavelength. A rigorous analysis reveals that refractive lenses become efficient at wavelengths $\lambda < 0.5$ nm due to strong absorption. Fabrication of surfaces with such radii is the goal of modern microelectronic technologies. And, indeed, these lenses have been made relatively recently, despite the fact that they had been proposed more than 100 years ago [38].

A significant improvement in spatial resolution became possible owing to the advancement of the fabrication technology of Fresnel zone plates (FZPs) transparent in the SXR range [39]. In accordance with the Rayleigh criterion, the FZP resolution (δx) is defined by the numerical aperture NA and the wavelength λ and, in the case of incoherent illumination, has the form

$$\delta x = \frac{0.61\lambda}{\mathrm{NA}} = 1.22\,\mathrm{d}r_n\,, \qquad (1)$$

where $\mathrm{d}r_n$ is the width of the outermost zone of the plate.

The numerical aperture of an FZP employed for high magnification is expressed in terms of the outermost zonewidth and the wavelength:

$$\mathrm{NA} = \frac{\lambda}{2\mathrm{d}r_n}\,. \qquad (2)$$

The focal distance f_1 for the first diffraction order, expressed in terms of the radius r_n and the outermost zone width $\mathrm{d}r_n$, the numerical aperture NA and the wavelength λ takes the form

$$f_1 \simeq \frac{r_n}{\mathrm{NA}} = \frac{2\mathrm{d}r_n\, r_n}{\lambda}\,. \qquad (3)$$

For instance, for a gold FZP with a record narrow outermost zonewidth $\mathrm{d}r_n = 15$ nm and $r_n = 15$ μm [40], the focal distance is about 200 μm at $\lambda = 2.3$ nm.

The efficiency of an imaging SXR FZP, which is defined as the fraction of incident radiation transmitted through the FZP, may be as high as 23% for an Ni FZP with zones parallel to its optical axis [41], and as high as 60% in the case of inclined zone geometry (similar to the blaze angle with diffraction gratings) [42]. In the experiments, however, the energy efficiency T of a phase plate with parallel zones for an outermost zonewidth $\mathrm{d}r_n = 30$ nm does not exceed 9% [41]. For an amplitude gold plate with the narrowest zonewidth $\mathrm{d}r_n = 15$ nm, the efficiency comprised 4% at a wavelength $\lambda = 2.3$ nm, taking into account the absorption in the support membrane [40]. Requirements imposed on the resolution of condenser zone plates are less stringent, and therefore use can be made of zone plates with a wider outermost zone. This permits raising the efficiency to 8–10%. Therefore, the overall efficiency of a system comprising a condenser zone plate and an imaging one may be estimated at 0.3–0.4%.

Among FZP features is a strong chromatic aberration, which requires a high monochromatization of the probe beam (the degree of monochromaticity must be no less than the number of Fresnel zones: $\lambda/\Delta\lambda \approx N \sim 500-1000$). This results in an additional loss in the beam intensity. Furthermore, high-resolution imaging FZPs are characterized by a small geometrical aperture (diameters smaller than 100 μm) [40, 43], with the consequential short focal distances (hundreds of micrometers), which shorten with increasing wavelength. This may be a hindrance to the practical employment of FZPs in the long-wavelength ($\lambda > 3$ μm) part of the SXR range. This is the reason why, despite the obvious progress in FZP fabrication technology (in particular, with its use it has been possible to achieve a resolution of about 15 nm in the vicinity of a 2-nm wavelength [40]), research in the area of soft X-ray microscopy has heretofore been limited to a small number of synchrotron laboratories.

For other applications in practical demand, like nanolithography or astronomy, FZPs are hardly utilized.

3. Multilayer interference structures for soft X-ray and extreme ultraviolet radiations

With the advancement of the synthesis technology of multilayer interference structures (MISs) with ultrashort (1–3 nm) periods, a realistic alternative to zone plates evolved for imaging with a high spatial resolution. The advent of X-ray multilayer optics may be regarded as one of the revolutionary nanotechnologies of the end of the 20th century. During the past 30 years, the MIS application area has widened manifoldly, and the majority of functions of conventional optics (collimation, focusing, imaging, radiation polarization) became also accessible in the SXR and EUV ranges.

X-ray multilayer mirrors comprise periodic structures consisting of material layers with different optical constants, by analogy with interference mirrors for the optical range. The characteristic features of X-ray mirrors are their extremely short (down to 1 nm) periods (in accordance with

the Bragg condition, the period of a structure consisting of two films is approximately $\lambda/2$ at normal incidence), a large number (up to 1000) of periods, and a strong radiation absorption in practically all materials. The need for the large number of periods stems from the low reflectivities of a single interface:

$$R_{1,2} \approx \left| \frac{\varepsilon_1 - \varepsilon_2}{4} \right|^2 ,$$

where $\varepsilon_{1,2}$ are the permittivities of the film materials. In the example with a silicon lens discussed above, the reflectivity R of the vacuum–silicon interface at a wavelength of 1 nm is equal to 2×10^{-8}. Even for so heavy a material as Au, the magnitude of R does not exceed 6×10^{-7}.

The problems of the physics of multilayer structures and interlayer boundaries, the methods of deposition and diagnostics of such structures, and their applications are discussed at length in review papers and monographs [32, 39, 44–46]. In this review, we dwell only on the key problems concerning ultrashort-period MISs intended for diffraction quality optics.

In the selection of MIS materials pairs for solving concrete problems, we are guided by the following main considerations. First, the optimal combination of materials optical constants has to be selected to maximize the reflection coefficient at a given wavelength. Second, the chemical interaction of the layer materials should be minimal, so as not to lower the optical contrast at the interfaces. Third, the layer materials should be deposited on substrates by vacuum deposition techniques, and they should grow without a noticeable development of film surface roughness. The problem is complicated by the fact that the physicochemical properties of superthin layers may be significantly different from the properties of a bulky material, so that a complex investigation is required in the selection of a new material.

In the early work, the selection of MIS materials was based upon considerations of maximizing the jump in the optical density of (material with a high atomic number Z)/(a low-Z material), for instance Au/C, W/C [39, 44, 47]). More recently, an approach whereby a material whose K or L absorption edge wavelengths are slightly shorter than the working wavelength is selected for a weakly absorbing material turned out to be more fruitful. Optimally, the working wavelength must correspond to the region of anomalous dispersion of the material: in this case, it exhibits minimal absorption and a maximal refractive index which exceeds unity in some cases [30, 31].

The selection of a strongly absorbing material comprises a compromise between the radiation absorption and the electron density jump at the interface. This approach is well illustrated by Cr/Sc MISs. Chromium ($Z = 24$) and scandium ($Z = 21$) are closely located in the Periodic Table of the elements and they differ little in electron density. However, in the region of anomalous dispersion of scandium in the neighborhood of the L_{III} absorption edge ($\lambda_L = 3.11$ nm), where the real part of its permittivity may be greater than unity and chromium possesses a weak absorption, this pair of materials exhibits the highest reflectivities. Beginning with the first studies of such mirrors [51, 52], which were extensively continued later on [53–55], just chromium was employed as a pair material for scandium, as the least interacting with the latter. As a matter of fact, scandium-based MISs with other transition metals have not been studied, and the demand is ripe for these investigations to optimize the multilayer optics for X-ray microscopes.

Table 1. Characteristics of periodic multilayer Cr/Sc mirrors in the spectral region of anomalous dispersion of scandium.

d, nm	N	λ, nm at $\theta = 85.6°$	$\lambda/\Delta\lambda$	R, %
1.57	250	3.142	263	10.8
1.58	250	3.155	246	9.7
1.64	250	3.272	271	7.4
1.69	230	3.358	231	6.5
1.70	250	3.373	245	6.7

To date, there is a limited set of materials pairs satisfying the requirements listed above. Among the most perfect short-period mirrors, mention should be made of a W/B_4C MIS [48–50], which may be used near the K absorption edge of oxygen ($\lambda \geqslant 2.36$ nm). However, even in the region $\lambda > 3.1$ nm, a significantly higher reflectivity is exhibited by scandium-based MISs. The measured characteristics of Cr/Sc MISs [46, 56], which demonstrate the behavior of the peak of reflectivity R in the region of anomalous dispersion of scandium, are collected in Table 1. The observed lowering of the reflectivity with increasing wavelength should be taken into account in the design of real optical systems. The lowering of reflectivity due to the impairment of optical constants is partly compensated for by an increase in the MIS period and the consequential weakening of the roughness effect on the reflectivities.

In principle, normal-incidence Cr/Sc mirrors possess reflectivities of about 10% up to $\lambda \approx 6$ nm; however, MISs based on carbon layers are optimal for the $\lambda > 4.4$ nm spectral region, behind the K absorption edge. Cr, Fe, and Co have been used as pair materials with carbon, although the majority of experiments have been carried out with Cr (a paramagnetic material), which is easily sputtered by the magnetron technique. It is valid to say that, as in the case with scandium, the selection of the optimal pair material for carbon has not been completed to date, and corresponding research is called for.

Figure 1 depicts the calculated and experimental reflectivities of several of the most promising MISs in the 2.3–20 nm

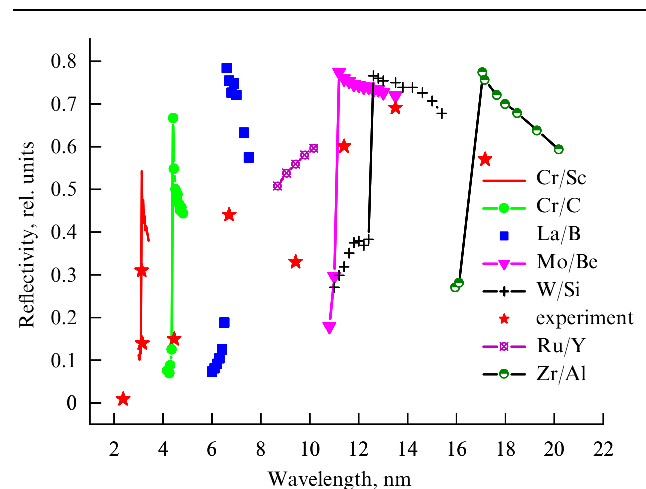

Figure 1. Calculated (lines with symbols) and experimental (stars) reflectivities of the most promising normal-incidence MISs.

Table 2. Reflection characteristics (calculations and experiment) of normal-incidence multilayer mirrors in the 2.3–17.4 nm wavelength range.

λ, nm	MIS	d, nm	N	φ_{Br}, deg	$\lambda/\Delta\lambda$	R_{ex}, %	$R_{ex}\,\Delta\lambda$, nm	R_{id}, %	References
2.36	W/B_4C	1.17	500	90	262	0.63	5.7×10^{-5}	18	[122]
3.14	Cr/Sc	1.56	400	85	263	15	1.8×10^{-3}	46	[54]
4.47	Co/C	2.26	200	85	153	14.8	4.4×10^{-3}	38	[123]
	Cr/Sc	2.21	200	85	186	7.5	1.8×10^{-3}	24	[46]
6.7	La/B_4C	3.39	150	80.5	120	40	2.2×10^{-2}	65	[68]
9.34	Ru/Y	4.75	100	80	60	33.5	5.2×10^{-2}	48	The present authors (2009)
11.34	Mo/Be	5.74	70	85	38	70.2	2.1×10^{-1}	75	[124]
13.5	Mo/Si	7.0	50	85	26	70.0	3.6×10^{-1}	73	[125]
17.35	Zr/Al	8.7	50	85	29	56.0	3.4×10^{-1}	75	[126]

Notes: λ — wavelength, d — multilayer structure period, N — number of periods, φ_{Br} — Bragg's angle, the quantity $\tan(\varphi_{Br})/\Delta\varphi_{Br} = \lambda/\Delta\lambda$ characterizes the selectivity of a multilayer dispersion element, R_{ex} — measured reflectivity, and R_{id} — reflectivity calculated for an ideal structure.

wavelength range, which characterize the current state-of-the-art in the synthesis technology of SXR and EUV normal-incidence mirrors. A more complete dataset for MISs is collated in Table 2. The multilayer mirror reflectivities obtained experimentally at the short-wavelength limit of the spectral range under consideration, $\lambda = 2.3$ nm, do not exceed 1%. As the working wavelength increases, the reflectivities exhibit a natural growth and amount to 70% in the 13-nm region, which is also attended by a decrease in spectral selectivity of the mirrors by more than an order of magnitude. In this case, the real reflectivity of multilayer mirrors, especially in the short-wavelength region, significantly differs from the reflectivity calculated for ideal structures with zero interplanar roughnesses.

The mirror reflectivities reached permit even now their efficient utilization, at least in the EUV range. However, it is well to bear in mind that optical systems with a high spatial resolution normally comprise no less than two elements and sometimes even more, and their efficiency lowers drastically already for an insignificant decrease in the reflectivities of individual mirrors. In the short-wavelength region, the mirror reflectivities are several times lower, and in the $\lambda \approx 2$ nm region even orders of magnitude lower, than the theoretical limit. That is why the key problem of X-ray multilayer optics involves increasing the reflectivity of MISs.

An especially strong effect on the reflecting characteristics of short-period MISs is exerted by the smearing-out σ of the interfaces between adjacent layers. The Fresnel reflectivity of a 'nonideal' interface in a Bragg resonance may be written down in the form $r_F \cong r_{F,\,id} \exp(-2\pi^2\sigma^2/d^2)$, where $r_{F,\,id}$ is the reflectivity of an ideal interface, and d is the structure period. One more negative consequence of the existence of transition interlayer boundaries is an increase in X-ray extinction length in an MIS, resulting in an increase in the number of reflecting layers, a narrowing of the spectral reflection band, and, accordingly, an additional lowering of integral reflectivities [57]. The interlayer regions in MISs are formed both by truly geometrical irregularities of the interfaces between layers and by diffusion and chemical interaction of the layer materials. The geometrical irregularities are, in turn, determined both by the initial substrate roughnesses and by growth roughnesses, which depend on the layer materials and the MIS deposition technology. Typical characteristics of mirrors of the SXR spectral domain are given in Tables 1 and 2.

Therefore, increasing the MIS reflectivities and advancing into the short-wavelength domain are closely related to the interface quality problem. To solve this problem requires developing technological MIS growth procedures with interfaces as abrupt as possible. It is also required to concurrently develop MIS diagnostic techniques which make it possible to investigate the fine structure of transition layers and separate the contributions from layer materials mixing and the truly geometrical irregularities, and to study the correlation between interlayer roughnesses and substrate roughnesses throughout the range of the spatial frequencies that define the reflectivities and imaging properties of MISs.

Although the properties of MIS interlayer roughnesses and their correlation with substrate roughnesses have been much studied [58–66], this problem has not been posed so broadly. In this connection, mention should be made of Ref. [50], where it was possible to separate the contributions from diffusive mixing and interlayer roughness in short-period W/B_4C MISs, proceeding from the analysis of the angular dependences of specular and diffuse scatterings of hard X-ray radiation. Despite the fact that the applied technique 'works' only in the analysis of MISs with fully longitudinally correlated layer boundaries, it has allowed obtaining several interesting physical results. Figure 2 displays the measured dependences of the total width σ of the transition zone, the interlayer roughness σ_r, and the mixing depth σ_m on the structure period for a series of MISs. From the resultant dependences, one can draw the following conclusions. First, as expected, the mixing depth, which is defined by mutual diffusion and 'ballistic' mixing of materials at the interfaces (atoms and ions with energies above 10 keV are present in the condensate stream), is hardly dependent on the MIS period. Second, the roughness σ_r varies slightly for long periods and begins to increase sharply from periods $d \approx 1.1-1.2$ nm. The most plausible explanation of this roughness behavior is related to the violation of layer continuity, when the average layer thickness corresponds to 0.4–0.6 nm. Third, the greater contribution to the transition

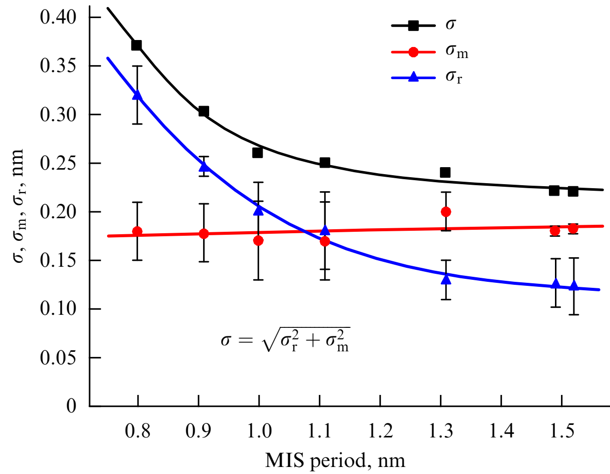

Figure 2. Transition region width σ, interlayer roughness σ_r, and mixing depth σ_m as functions of d for a series of W/B_4C MISs.

zone width for MISs with periods $d > 1.1$ nm is not made by geometrical irregularities, as expected earlier, but by the mixing of layer materials, which is determined primarily by the energetics and chemical composition of the condensate.

By and large, these investigations revealed that short-period W/B_4C structures possess perfect layer boundaries. Similar properties are also inherent in W/Si MISs with periods $d > 2$ nm. The investigations resulted in a significant advancement towards shorter-period MISs.

Another significant feature of superthin-film MISs is that the parameters of the heteroboundaries in the unit cell of an MIS may be substantially different owing to the difference in the physicochemical properties of the materials. In many MISs utilized as X-ray optical elements, the asymmetry of layer interfaces is moderate, and the employment of diagnostic methods developed for MISs with symmetric boundaries does not lead to significant errors in determining the individual film thicknesses and densities, as well as the MIS effective interlayer roughness. In some cases, however, the asymmetry of layer interfaces may not be neglected. For instance, the asymmetry of electron density in the unit cell of an La/B_4C MIS is so large that conventional diagnostic techniques [32, 57, 67] do not make it possible, proceeding from reflectometry data, to adequately describe the MIS structure and predict the mirror reflectivities in different X-ray regions [68, 69].

The problem of the diagnostics of these structures arises from the fact that the asymmetric profile of the electron density [permittivity $\varepsilon(z)$] cannot be expanded into a Fourier series only in terms of cosines, as is done under the traditional approach (see, for instance, Refs [32, 57]):

$$\varepsilon(z) = \varepsilon_0 + (\varepsilon_1 - \varepsilon_2)\left\{\sum_{m=1}^{\infty} a_m \cos\left(\frac{2\pi mz}{d}\right) + \sum_{m=1}^{\infty} b_m \sin\left(\frac{2\pi mz}{d}\right)\right\}, \quad (4)$$

where d is the structure period, $\varepsilon_0 = \beta\varepsilon_1 + (1-\beta)\varepsilon_2$ is the permittivity averaged over the MIS, β is the fraction of the strongly absorbing substance in the period, and a_m and b_m are the real harmonic amplitudes normalized to $(\varepsilon_1 - \varepsilon_2)$, which are determined only by the geometry of the problem and are independent of the permittivities of the MIS substances. The reflectivity of the MIS in the mth peak is defined by the expression

$$r_m = \frac{\mathrm{i}\varDelta_{\pm m} \tanh\left(Nd^2\sqrt{\varDelta_{+m}\varDelta_{-m} - u_m^2}/2\pi m\right)}{\sqrt{\varDelta_{+m}\varDelta_{-m} - u_m^2} - \mathrm{i}u_m \tanh\left(Nd^2\sqrt{\varDelta_{+m}\varDelta_{-m} - u_m^2}/2\pi m\right)}, \quad (5)$$

where $u_m = k_0^2(\varepsilon_0 - \sin^2\theta) - (\pi m/d)^2$, $\varDelta_{\pm m} = k_0^2(\varepsilon_1 - \varepsilon_2) \times (a_m \pm \mathrm{i}b_m)$, $k_0 = 2\pi/\lambda$ is the wave vector, and N is the number of MIS periods. As is evident from expression (5), both the sine and cosine constituents of $\varepsilon(z)$ make contributions to the reflectivity. Their independent determination requires measurements of the modulus and phase of the reflection coefficient, which is highly problematic in practice, and especially so under laboratory conditions.

As shown in Ref. [69], the permittivity profile for a trapezoidal electron density distribution with different slopes of the flat sides, and assuming equal optical layer thicknesses in the MIS period ($\beta = 0.5$), can be represented by an odd function and expanded into a series in terms of only sines ($a_m^{\mathrm{norm}} = 0$). This permitted constructing the profiles of electron density in La/B_4C MISs with different periods (Fig. 3). One can see from this figure that the real transition zones are rather wide, about 1 nm, and are hardly dependent on the MIS period. Substitution of this profile into the Parratt recurrent relations [70] yielded good agreement between experimental and theoretical reflection coefficients in different X-ray regions. This approach has made it possible to explain the reason for the insufficiently high SXR reflectivity of La/B_4C MISs, observed by practically all researchers concerned with MISs based on this materials pair [46, 48, 71–73]. The main reason lies with the anomalously strong

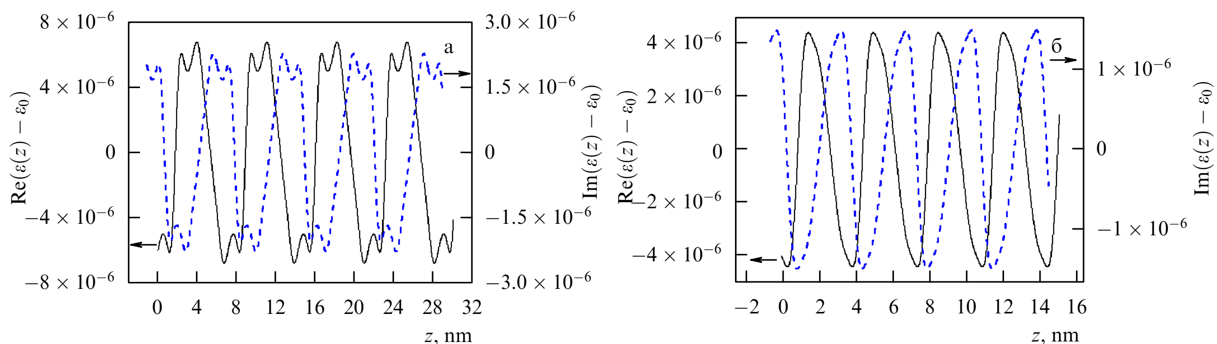

Figure 3. Permittivity profiles reconstructed from the amplitudes of Fourier harmonics in the framework of the 'trapezoidal' model for La/B_4C MISs: (a) $d = 7.1$ nm, and (b) $d = 3.5$ nm.

chemical and diffusion interaction between lanthanum and boron.

At the present time, the La/B_4C pair is regarded as the virtually alternative-free basis for multilayer optics of the $\lambda \approx 6.7$ nm spectral region, which is of special interest for next-generation X-ray nanolithography [14, 15]. That is why the development of the diagnostics of MISs with asymmetric interlayer interfaces have turned out to be helpful both in the advancement of MIS deposition technology and in the search for superthin barrier layers which impede the lanthanum–boron interaction in an MIS.

Despite the seemingly stringent limitations (the permittivity profile is a nonisosceles trapezoid, with the parameter $\beta = 0.5$), the method described above may be applied to the structural study of the period in any MISs with asymmetric transition boundary layers. When the electron density profile at the interfaces is significantly different from the linear one, this method may be regarded as a first approximation, and further fitting may be accomplished using an algorithm like the Parratt recurrent relations.

It is noteworthy that, although some problems both in the diagnostics and in the deposition technology of efficient normal-incidence MISs still exist, even today the majority of the aforementioned goals are solved with their help, at least in the $\lambda > 3$ nm wavelength domain.

4. Methods for investigation and precision correction of the shape of optical elements with supersmooth surfaces

The key factors that had long deterred the development of precision imaging SXR optics were the stringent requirements on the shape of mirror surfaces and on the aberrations of a lens as a whole. According to the Marechal criterion, to achieve diffraction quality imaging the square root of the rms aberration of a projection lens must satisfy the criterion $RMS_{obj} < \lambda/14$, where λ is the radiation wavelength. In the SXR region, this amounts to 0.15–0.30 nm. It is pertinent to note that the requirement imposed on RMS_{obj} is inherently integral: the wavefront aberrations are integrated over the entire spectrum of spatial frequencies, from the macroscopic diameter of the mirrors to half of the radiation wavelength ($\nu \sim 10^{-6} - 10^{3}$ μm^{-1}); in so doing, the departures of the shape from the prescribed one are treated as low-frequency irregularities with spatial frequencies $10^{-6} - 10^{-3}$ μm^{-1}. The key problems are, therefore, related to optical surface shape measurements with an accuracy of about 0.1 nm and the fabrication of such optical elements. The task is additionally complicated by the fact that the optics is, as a rule, aspheric in shape.

Traditional interferometric methods of monitoring the shape of optical surfaces, in which a wavefront produced in the reflection from a reference surface is employed as the reference wavefront [74], possess a high (over $\lambda/1000$) sensitivity to variations of the shape of wavefronts. In this case, however, the absolute accuracy of measurements of real front shapes is no higher than $\lambda/20 - \lambda/50$ [75] (λ is the working interferometer wavelength). This is related to the quality of reference surface shapes, as well as to the specific design of interferometers, in which light beams pass through several optical elements to acquire additional uncontrollable phase incursions [76].

The application of traditional methods of measuring roughness in the medium- and high-frequency ($\nu \sim 10^{-3} - 10^{3}$ μm^{-1}) ranges (atomic-force and optical interference microscopies, diffuse scattering of a hard X-ray radiation) also called for a substantial revision of the real capabilities of these techniques in the study of supersmooth surfaces [77, 78]. To realize the feasibility of ultrahigh precision measurements of a surface shape required abandoning the traditional method of instrument calibration with the help of reference surfaces and developing methods reliant on basic physical principles, when the main instrument (method) characteristics can be measured in a physically lucid experiment with the capability of making a reliable estimate of the measurement accuracy. Interferometry with a diffracted reference wave, which was proposed in 1933 [79] and was not called for until 1996 [80], became such a method for certifying optical surface shapes. The heart of the method lies in the formation of a reference spherical wave due to light diffraction by a small aperture. The solution of the classical problem in light diffraction by a hole in a zero-thickness screen with an infinite conductivity shows that the phase surface of the wave is an 'ideal' sphere within the diffraction maximum (the angular width of the maximum is about $\pm\lambda/d$, where d is the hole diameter).

The number of suchlike interferometers in the world with working wavelengths of 633, 530, and 13.5 nm amounts to about ten. The authors of Ref. [81] reported the attainment of a wavefront aberration measurement accuracy of about 0.08 nm over a numerical aperture $NA \approx 0.1$. Unfortunately, it is regrettable that, with the exception of Refs [76, 77, 81], the data on the measurement accuracy furnished by the instruments are either not given at all or the figures are given without a description of the accuracy measurement method, which casts serious doubts upon them.

Interferometers with diffracted reference waves have not yet gained wide acceptance because of the alignment complexity and the uncontrollable effect of primary optics aberrations on the quality of the diffracted wave front [82]. In addition to technical difficulties, the authors of Refs [83, 77] revealed several physical effects which adversely affected the quality of the diffracted wave front.

Figure 4 shows the geometry of the problem (a) and the plots illustrating the effects of finite thickness (Al film, Fig. 4b) and the screen material (Fig. 4c) on the aberration of the diffracted wave in relation to the observation angle. The entire phase incursion is gained over the skin layer thickness $\delta \approx c/\Omega_p \approx 10 - 20$ nm for good conductors characterized by plasma frequencies $\Omega_p \sim 10^{16}$ rad s^{-1} (c is the speed of light in vacuum). From the geometry of the problem presented in Fig. 4a, it is evident that the greater the polar angle, the more important the role of the film material, because the radiation propagates partly through an optically denser material, which results in a greater phase incursion. Another effect responsible for the distortion of the phase front is the excitation of plasmon–polariton and waveguide modes in the proximity to the hole.

All these effects have the consequence that the declared reference wave aberrations of about 0.1 nm are provided within relatively small numerical apertures of about $NA \approx 0.1$. That is why when certifying large-aperture optical elements one is forced to 'stitch' the zonal measurement data, which complicates the measurement procedure and entails additional errors.

These problems are partly solved when single-mode fibers with an output aperture decreased to a subwavelength size are employed as the source of a reference spherical wave (2008,

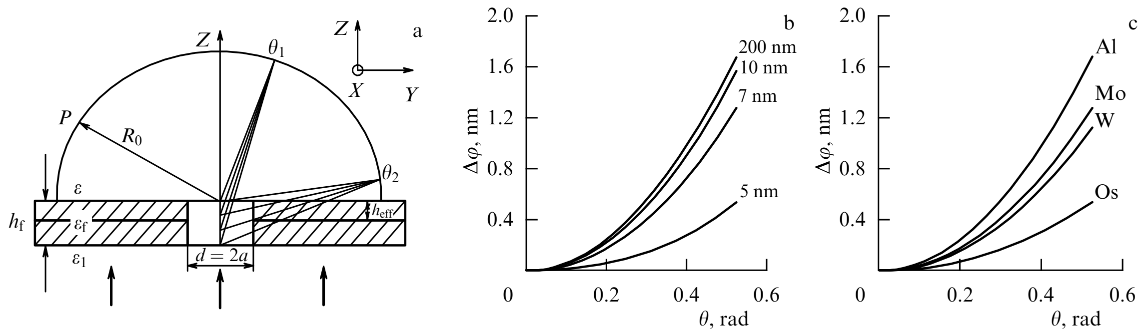

Figure 4. (a) Geometry of the problem: h_f — film thickness, h_{eff} — effective film thickness (characterized by the skin depth for a specific material), d — hole diameter, ε, ε_1, and ε_f — media and film permittivities. (b) Phase incursion $\Delta\varphi(\theta) = (\varphi(0) - \varphi(\theta))\,\lambda/2\pi$ as a function of the polar angle plotted for different thicknesses of aluminium film ($\varepsilon_{Al} \approx -54.2 - 21.8i$), the radius of the hole in the film $d = 150$ nm. (c) Phase incursion as a function of the polar angle plotted for various materials.

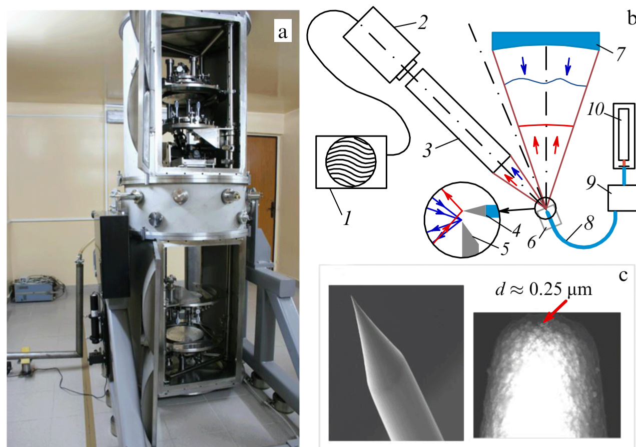

Figure 5. Photograph (a) and optical diagram (b) of a vacuum interferometer with a diffracted reference wave, and electron microscope image (c) of the source of the reference spherical wave based on a single-mode optical fiber with an output aperture narrowed to a subwavelength size. *1* — computer, *2* — CCD (charge-coupled device), *3* — viewing system, *4* — spherical wave source, *5* — plane mirror, *6* — precision three-axis stage, *7* — concave surface under investigation, *8* — fiber, *9* — polarization controller, and *10* — laser.

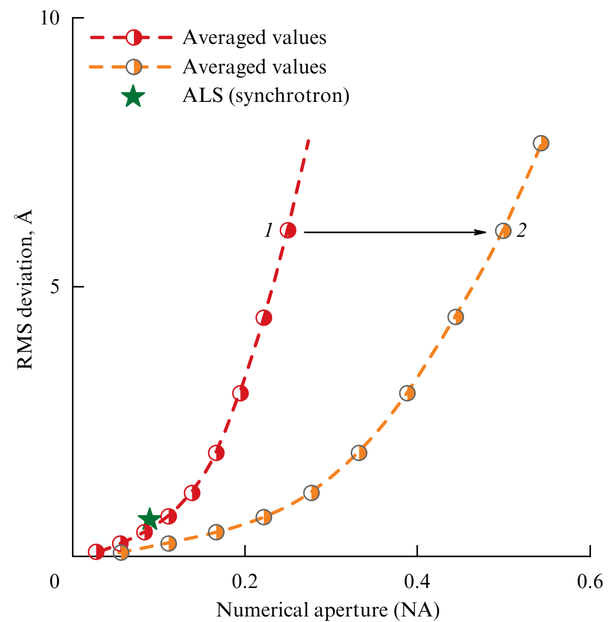

Figure 6. Comparison of the accuracy of measurements using the interferometer developed by the present authors (curves with symbols) and the ALS interferometer (star) versus numerical aperture. Curve *2* corresponds to the aberrations of the wave generated by the optical fiber source of the spherical wave.

IPM of the RAS) [84]. An electron microscope image of the fiber is given in Fig. 5c. The aberrations of the generated wave were experimentally investigated by Young's method, where a study was made of the interference of the waves produced by two similar sources. The experimental technique is described at length elsewhere [81, 84]. Curve *1* in Fig. 6 corresponds to reference wave aberrations in the interferometer (schematically shown in Fig. 5b), when the component under investigation and the recording system are illuminated by the side parts of the source front. Curve *2* corresponds to the aberrations of the diffracted wave generated by this source. The measurements were carried out at a wavelength of 532 nm, the 2nd harmonic of an Nd:YAG laser. The star marks the record aberrations of a wave generated using the traditional source of a spherical wave — a hole in an opaque screen (the measurements were made at a wavelength of 13.5 nm with the ALS synchrotron (Berkeley, USA)). For the same numerical aperture, as is evident from the figure, the fiber-based source possesses an aberration that is two times smaller. Furthermore, because of the short operation wavelength, the working aperture of the ALS interferometer is limited to a value of NA ≈ 0.1, while the optical fiber source exhibits a subnanometer aberration for NA > 0.5. The advantages of this way of forming a reference spherical wave arise from the convex shape of the source surface, the absence of a screen on the rare of it, and the high intensity of the diffracted wave, because advantage is taken of the well-elaborated technique of introducing the radiation into a waveguide core 4 μm in diameter.

Using this spherical wave source as the base, a vacuum interferometer was commissioned at the IPM of the RAS [85], which has been successfully operated for more than three years. A photograph and an optical diagram of the instrument are given in Figs 5a and 5b.

Despite the impressive success of interferometry with a diffracted reference wave, the problem of certifying optics with subnanometer precision may, strictly speaking, be considered as being solved only for spherical surfaces and lenses. In the study of aspherical components, one is forced to

resort to wavefront correctors transforming spherical wavefronts to aspherical wavefronts close in shape to the surface under investigation [86]. The inclusion of wavefront deformations introduced by correctors is a separate and rather intricate task. The sole exception is provided by ellipsoids: owing to the existence of two foci, they may be certified using an interferometer (designed by the present authors) without the employment of correctors (the sources of the reference and working fronts are located at the ellipse foci).

The emergence of metrology lent impetus to the development of methods for fabricating optical element surfaces of various shapes with subnanometer accuracy. Such optical elements are fabricated in two steps. In the first, a supersmooth surface is prepared with the use of conventional polishing techniques and certification of shape and roughness. In the second step, the shape is corrected to subnanometer deviations from the desired shape with the application of local ion-beam etching and/or vacuum thin-film deposition.

The key requirement for the correction procedure is to retain the surface roughness at the initial, atomically smooth level. This fostered a broad front of research into studying the effect of technological process parameters on the surface roughness. As shown by an analysis of a large number of studies, the resultant experimental data are highly contradictory. Notably, some authors recommend performing ion etching at small grazing angles of incidence or ion (neutral atom) energies above 1 keV; a strong dependence of etching parameters on the substrate material has been observed [87–89].

Investigations of the influence of ion beam parameters and the ion etching modes on the surface roughness performed recently at the IPM of the RAS showed that the roughnesses of the supersmooth surfaces of Cr/Sc multilayer structures and fused silica as functions of ion energy remained at the initial level (Fig. 7), when the ion beam is incident at angles close to the surface normal. As this takes place, the energy of the ions (or neutral atoms) should not exceed 200 eV in the event of Cr/Sc etching, and 800 eV in the case of fused silica. By contrast, when the ion beam was obliquely incident on the surface, the irregularities were practically always observed to develop throughout the spatial frequency spectrum (Fig. 7b).

This behavior of a surface roughness in ion beam etching is qualitatively attributable to the fact that at near-normal incidence the depth of ion penetration into a solid increases, with the consequential lowering of the energy fraction transferred to near-surface atoms. In this case, only the least bound atoms detach from the surface (etching), and the peaks thereby smooth out or, at least, surface irregularities do not develop. A similar effect is observed in the etching with low-energy ions (atoms).

In our view, the indicated difference in the results of studies of roughness evolution under ion etching is due to the not-well-established method of certifying roughnesses in the medium frequency range ($\nu \sim 10^{-3} - 10^{-1}$ μm^{-1}), which make the greatest contribution to the rms surface roughness. To measure these irregularities, use is made of optical interference microscopy, whose suitability for studying supersmooth surfaces is in serious doubt [78]. In this connection, mention can be made of two techniques which allow most reliably estimating the integral substrate roughness in the region of high and medium spatial frequencies by analyzing the angular dependences of specular hard X-ray reflection coefficients for substrates [90] and for short-period multilayer

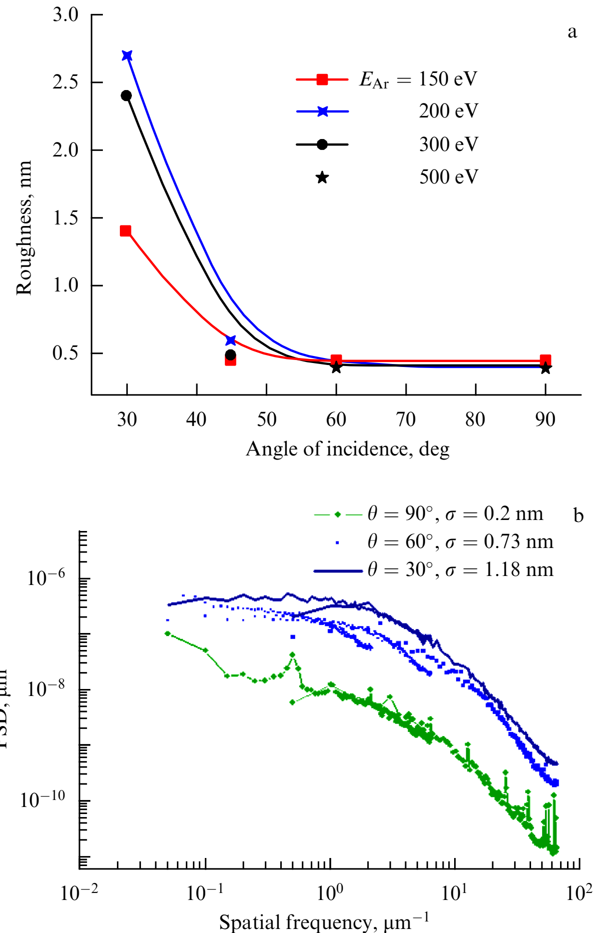

Figure 7. (a) Fused silica surface roughness as a function of the angle of incidence of argon atoms accelerated to energies E_{Ar} = 150, 200, 300, and 500 eV, and (b) dynamics of power spectral density (PSD) functions of the roughness in the etching of Cr/Sc MISs.

mirrors deposited on them. For the mirrors, the influence of substrate roughness is enhanced manyfold owing to the interference of waves reflected from a large number of interfaces. In Ref. [91], a clear correlation was shown between the reflectivities of multilayer mirrors deposited on the etched substrates and the surface roughnesses given in Fig. 7.

A more complicated situation is observed in the etching of single-crystalline silicon, which shows, as in the case with silica and Cr/Sc, a retention or improvement of roughness at near-normal angles of incidence [89]. However, the angular range wherein this effect is observable turns to be very narrow: $50° - 60°$ [89, 92]. As this takes place, an additional relief in the form of waves with a period of $L \sim 20$ μm appears on the surface (Fig. 8). And though the relief amplitude (h) amounts, as a rule, to a fraction of a nanometer, this may give rise to an appreciable angular error ($h/L \sim 10^{-4} - 10^{-5}$) for the X-ray radiation wavefront reflected from the surface.

It is noteworthy that the method of precision substrate shape correction for X-ray imaging optical elements by local ion-beam etching has been reliably elaborated for materials like Zerodur and ULE ceramics (Ultra-Low Expansion ceramics having a minimal thermal linear expansion coefficient, TLEC $\approx 10^{-8}$ K^{-1}) [93], fused silica (the most widespread material for X-ray optics, TLEC $\approx 10^{-7}$ K^{-1}), and the

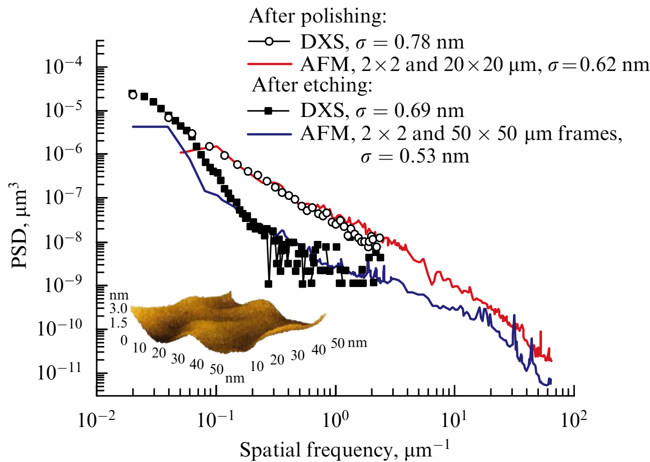

Figure 8. PSD functions of the roughnesses of single-crystalline silicon prior to (upper curve) and after (lower curve) etching by Ar^+ ions, and AFM surface image after the etching. DXS — diffuse X-ray scattering.

Table 3. Best results in the effective roughness of polished substrates measured in the frequency range $\Delta\nu = 0.02-64\ \mu m^{-1}$. The table was compiled on the basis of several hundred tests of substrates from tens of various manufacturers.

Substrate material	σ_{eff}, nm
Si (General Optics, USA)	0.43
Si (South-East Asia)	0.22
Si (South-East Asia)	0.62
Silica (General Optics, USA)	0.37
Silica (General Optics, USA)	0.33
Silica (Kompozit, Moscow)	0.32
Cr/Sc MIS on Si (IPM of the RAS, N. Novgorod)	0.36
Zerodur (Edmund Industrial Optics, USA)	0.53
Sapphire (IC of the RAS, Moscow)	0.20

Cr/Sc multilayer structure. The last of these possesses unique properties: retention of the initial substrate roughness, the possibility of chemical removal without impairment of the substrate surface, and controllable variation of mechanical stress, both in magnitude and in sign, by varying the Cr-to-Sc layer thickness ratio in the period [94].

At present, to the best of our knowledge, the entire technology cycle (metrology, superpolishing, and shape correction) required for producing substrates and ultrahigh-resolution projection lenses is being undertaken by ZEISS (FRG) and partly by General Optics (USA) and Nikon (Japan). In a laboratory version, this technology has been developed at the IPM of the RAS (Russia). The best results achieved in the polishing of substrates intended for optical (X-ray optical) applications are collected in Table 3. The measurements were made at the IPM by the methods of atomic-force microscopy (AFM) and hard X-ray diffuse scattering in the 0.02–64 μm^{-1} range of roughness spatial frequencies. Roughness cross-tests of several substrates performed at Rigaku Innovative Technologies, Inc. (Japan) amply bore out the results obtained at the IPM. As is evident from Table 3, the minimal roughness of 0.2 nm was obtained on polished single-crystalline silicon plates (100) manufactured in South-East Asia, and on sapphire substrates produced at the Institute of Crystallography (IC) of the RAS. The fused silica polishing procedure developed jointly by the Kompozit Co. (Moscow) and the IPM is a world state-of-the-art technology.

The methods developed for precision surface shape correction are also of interest in their own right, for instance, when it is required to make precisely shaped reference surfaces for conventional interferometers. Figure 9 displays the result of correction of local departures from the nearest sphere for a concave spherical surface 130 mm in diameter with a numerical aperture NA = 0.25. The initial surface departure from the ideal sphere was characterized by the maximal swing $P-V = 42.6$ nm ($P-V$ is the peak-to-valley amplitude) and an rms deviation RMS = 7.3 nm. Upon correction, the RMS value was improved by approximately an order of magnitude and was diminished to 0.6 nm, with $P-V = 7.3$ nm. The iterative correction procedure may be continued and the shape error significantly decreased.

The laboratory technology for making multilayer mirrors with an aspherical subnanometer surface shape accuracy was developed at the IPM of the RAS for making the elements of X-ray space telescopes and the projection lens of a 13.5-nm wavelength nanolithography tool. In several problems typical, for instance, to X-ray astronomy, the greatest departure of the aspherical surface from the nearest sphere is not very large: ≈ 0.5 μm. In this case, however, the substrate surface

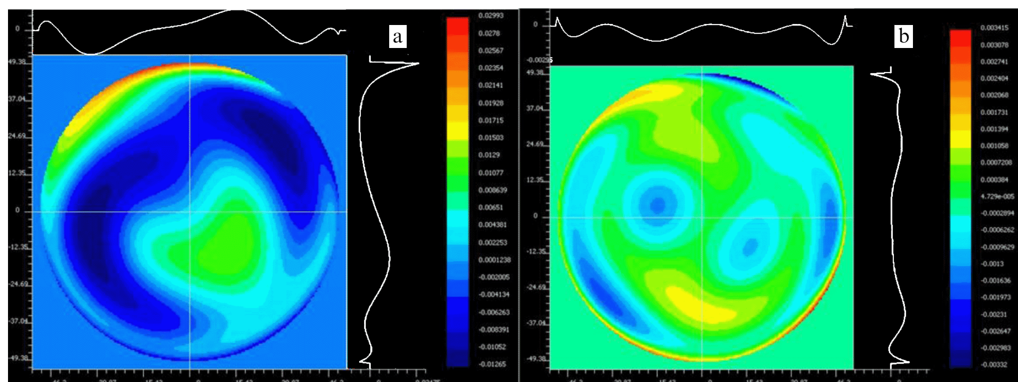

Figure 9. Result of correction of local surface departures from the nearest sphere for a concave spherical substrate 130 mm in diameter with a numerical aperture NA = 0.25: (a) initial map ($P-V = 42.6$ nm, RMS = 7.3 nm), and (b) after 12 corrections ($P-V = 7.3$ nm, RMS = 0.6 nm).

for the multilayer mirror has to be supersmooth and produced with a nanometer-level accuracy, and the simplest way of making the substrate involves fabrication of the nearest spherical substrate with a supersmooth surface, which is then made asphérized by way of a local film or local ion-beam shape correction.

In the fabrication of the lens optical elements for projection EUV lithography systems or SXR microscopes, the magnitude of aspherical surface shape deviation from the nearest sphere ranges from several to tens of micrometers. In these cases, as a rule, a supersmooth surface is fabricated with a shape as close as possible to the desired one, and then a precision surface correction is carried out under a permanent monitoring of the shape and roughness. Figure 10 displays the map of surface shape departures from the desired shape for an aspherical concave mirror of an EUV nanolithography tool made at the IPM. The mirror's numerical aperture is NA $= 0.3$; the greatest departure from the nearest sphere is equal to 6.6 μm. The maximal swing of profile departures from the desired profile was within $P-V = 7.7$ nm, and RMS $= 0.9$ nm [95].

Low-energy ion etching modes were found for fused silica, whereat no surface roughness development was observed when etching to a depth of more than 10 μm. This fact opens the way to direct ion-beam asphérization of initially spherical substrates, bypassing the stage of mechanical 'light-tool' polishing or grinding. This method of asphérization should significantly improve the surface roughness in the medium-frequency range [93]. The technology of asphériza-tion of atomically smooth surfaces by ion beam etching is the technology of the immediate future.

In summary, it may be noted that the fabrication of precision EUV/SXR optical elements and optical systems at the IPM of the RAS relies on a purpose-made technological and measuring facility which comprises a high-transmission interferometer with a diffracted reference wave, techniques and equipment for measuring roughness and correcting surface shape, and deposition technologies and reflectome-try at the working wavelengths of multilayer mirrors for the entire SXR and EUV radiation range.

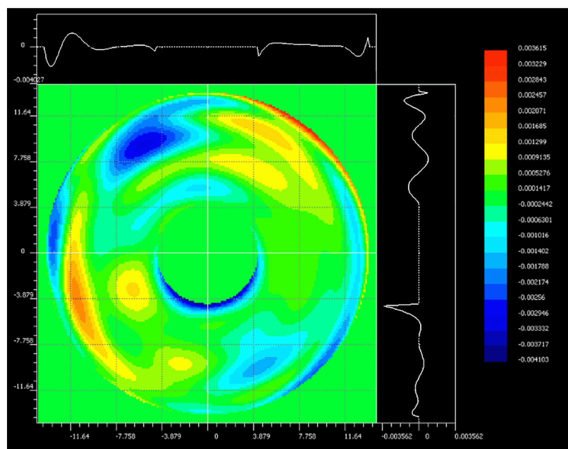

Figure 10. Surface map of an aspherical mirror with a numerical aperture NA $= 0.3$ and the greatest departure from the nearest sphere equal to 6.6 μm made at the IPM, RAS, for an EUV nanolithography tool. The maximal swing of profile departures from the desired profile falls within $P-V = 7.7$ nm, and RMS $= 0.9$ nm.

5. Applications of ultrahigh-precision X-ray optics

In this section, we consider several very interesting, in our opinion, applications of precision multilayer optics in the SXR and EUV ranges, in particular, projection EUV nanolithography, X-ray microscopy, astronomy, and the production of ultrahigh electromagnetic fields in the X-ray range. However, this selection of application areas is quite arbitrary, because precision optical systems comprising elements with supersmooth surfaces, i.e., with anomalously weak scattering and subnanometer shape accuracy (including aspherical ones), may be of interest for any spectral region. For instance, among these applications mention should be made of deep ultraviolet lithography lenses ($\lambda = 193$ nm) with a resolution of 20–30 nm, optical systems for high-resolution land surface satellite observations, and the formation of the base of next-generation standards that are 1–2 orders of magnitude more accurate than the presently existing standards of traditional interferometers.

5.1 Projection nanolithography

At present, it is generally recognized that projection EUV lithography at the wavelength $\lambda = 13.5$ nm is the most economically rational for the volume production of modern integrated circuits. And although several technical problems remain to be solved, it is anticipated that the 2012–2013 period will see the commencement of electronic chip produc-tion with element dimensions down to 22 nm [15]. In the future, the element dimensions may be decreased to 10 nm, when increasing the lens numerical aperture; upon further shortening the working radiation wavelength, for instance, to $\lambda = 6.7$ nm, the element dimensions may be brought down to 8 nm.

One of the key factors underlying the development of short-wavelength nanolithography is progress in the area of fabrication of ultrahigh-precision optics. Three projection nanolithography tools, the prototypes of industrial facilities (α-tools), which afford a resolution up to 22 nm for lines and up to 32 nm for circles, are presently operating in the world (Fig. 11) [96, 97]. To study photoresists and develop EUV lithography processing, use is made of several test stands with two-mirror projection lenses incorporating numerical aper-tures increased to NA $= 0.3$ [98].

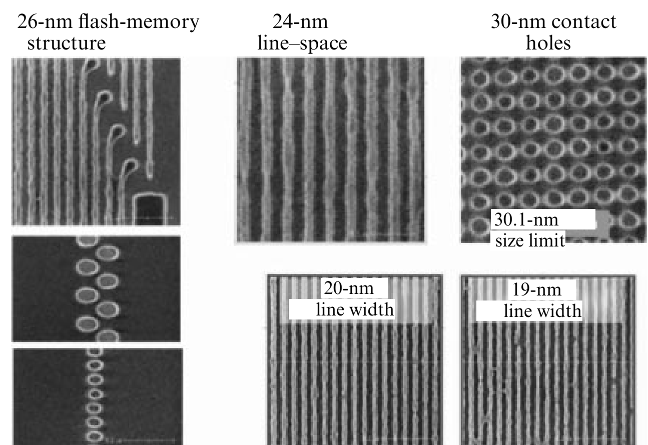

Figure 11. Topological patterns produced by EUV projection lithography with a six-mirror nanolithography tool (borrowed from Ref. [96]).

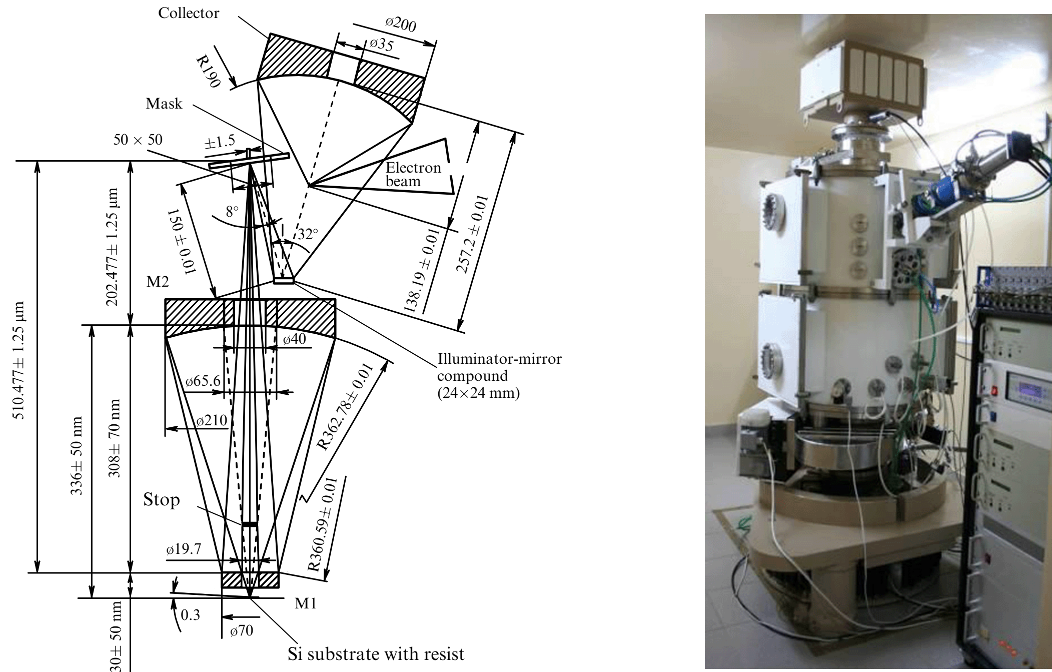

Figure 12. Optical diagram and photograph of the nanolithography multiplier tool developed at the IPM, RAS.

Requirements imposed on imaging optical elements and optical systems stem from the scanner resolution (16–22 nm). According to estimates, the admissible deformation of the wavefront transmitted through a projection lens should not exceed 0.6–0.9 nm. Assuming that the errors of different mirrors of the lens are independent, the admissible error of the aspherical surface shape for each mirror in a six-mirror lens is about $0.3-0.4$ nm.

Let us consider the main design principles of an EUV nanolithography tool by the example of a nanolithography multiplier stand with a working wavelength of 13.5 nm and an estimated resolution of 30 nm, which was designed and fabricated at the IPM, RAS in 2010 in the framework of a contract with 'Rosatom' State Corporation [99]. An optical diagram and photograph of the nanolithography tool are shown in Fig. 12. Employed for a radiation source are either a purpose-designed dismountable X-ray tube or, alternatively, a laser plasma source. The radiation in the spectral region $\lambda \approx 13.5$ nm is intercepted within a solid angle of ≈ 1.2 sr by a spherical collector with a reflective Mo/Si multilayer coating. The radiation reflected from the collector mirror is incident on an illuminator mirror consisting of 25 minimirrors with reflective Mo/Si coatings, which produces a uniform irradiation intensity distribution over a mask 3×3 mm in size. The properties and the method of fabrication of the illuminator mirror are described at length elsewhere [100].

The mask comprises an Mo/Si multilayer mirror coated with a layer absorbing the 13.5-nm radiation. Windows with the requisite pattern were made in this layer by electron-beam lithography and plasma-chemical etching. The on-mask pattern is imaged with a 1:5 demagnification on a plate with a photoresist with the help of a projection lens.

The projection lens is designed according to the Schwarzschild scheme and consists of two aspherical mirrors: a convex M1 mirror, and a concave M2 one. The aspherical shape of the mirrors affords its 3×3-mm field of view on the mask. (In this case, the term field of view is used in reference to the domain on the mask imaged by the projection lens with a resolution of 30 nm.) For more details about the lens properties as well as the methods of its fabrication and certification of wave aberrations, see Refs [85, 95].

Upon irradiating a part of the photoresist-coated plate by the requisite radiation dose (planned for mass production is a 5–10 mJ cm^{-2} dose), the photoresist-coated plate and, if need be, the mask may be transferred using 2D stages, and the irradiation procedure may be repeated. At the present time, the system of cooperative scanning of the photoresist-coated plate and the mask is lacking in the nanolithography tool under description, so that the tool operates in a multiplier mode, i.e., a nanostructure is formed and this pattern may then be multiplicated on larger plate areas.

The lens's depth of focus is about 100 nm, and the image quality is therefore extremely sensitive to deviations in the distances between the optical elements of the nanolithography tool, which automatically imposes strict limitations on the planeness of the surface mask and the photoresist-coated plate. This problem is especially acute for a 0.5–1.0-mm thick semiconductor plate, because its rigidity is not high enough. In the projection configuration involved, planeness is achieved by electrostatically pressing the plate onto a glass substrate which deflects from the plane by no more than 30 nm.

To provide diffraction image quality, the mutual positions of several optical elements in the projection scheme must be controlled to within ± 50 nm, or $\sim 10^{-7}$ in relative units, in the nominal values (see Fig. 12). For instance, when Invar with TLEC $\approx 10^{-6}$ K^{-1} is employed as a structural material, the configuration has to be temperature stabilized to within 0.1 °C to satisfy this constraint. This requirement is extremely hard to satisfy in practice because of local heat release in the operation of different units of the nanolithography tool. That is why, unlike traditional compound lenses, when the constituent optical elements (lenses) are assembled, aligned once, and then fixed in their working positions, in the case of SXR and EUV compound lenses it is required to permanently monitor the lens positions and align the lenses in the course of

operation, as well as to maintain the thermal stability of the entire projection optical system. In this nanolithography tool, the problem is solved by placing position sensors on the optical elements, whereas their coupled elements (in our case, these are the opposite plates of capacitive position sensors) are placed on the rods made of special glassceramics with TLEC $\approx 2 \times 10^{-8}$ K^{-1}.

To monitor and retain the mask and photoresist-coated plate positions at the nanometer level, a special system was invented — an autofocus, whose operating principle is widely used for monitoring the cantilever deflections in an atomic-force microscope, and which relies on the recording of reflected radiation by a four-section semiconductor diode. Depending on the plate displacement, the diode sector signals are redistributed between themselves.

To protect the optical system from vibrations, the test stand possesses several vibration suppression stages. At present, the stand has been placed in service, and a start has been made on the fabrication of nanostructures by EUV projection lithography.

In recent years, a wavelength in the vicinity of $\lambda \approx 6.7$ nm has been discussed as the working wavelength of lithography tools for further improving resolution to ≈ 8 nm [14, 15, 72]. Research is actively being pursued to study the feasibility of making efficient multilayer optics and the corresponding radiation sources for the 6.7-nm spectral region. In so doing, it is clear that a twofold wavelength shortening will call for the improvement of the methods of fabrication and characterization of the optics to also achieve a twofold increase in shape accuracy. The problem of achieving high reflectivities of lanthanum-bearing multilayer interference structures still remains to be solved [69, 101].

5.2 X-ray microscopy

Apart from a high spatial resolution arising from the short radiation wavelength, X-ray microscopy offers several unique advantages over other kinds of microscopy. Among the main advantages is a high absorption contrast which arises from the fact that this wavelength region contains the absorption K-edges of light elements (O, N, C), which form the basis of life, and the L-edges of K and Ca — the elements playing a crucial role in the formation of skeletal tissues.

Figure 13 depicts the spectral dependences of radiation penetration depth for the main biological substances: DNA, proteins, fats, water, etc. [102]. One can see from the figure that, first, water is sufficiently transparent in the 2–4-nm wavelength range to allow studying samples up to several dozen micrometers in thickness. Second, the path lengths in proteins and other organic substances amount, by contrast, to fractions of a micrometer, which underlies a high sensitivity to low carbon-bearing inclusions and, accordingly, provides a high contrast of X-ray images.

At wavelengths longer than 4.4 nm, prior to the absorption K-edge of carbon (the carbon window), a high contrast of biological sample images is observed in paraffin. This property is demanded in histological studies, when a sample under examination is hermetically sealed in paraffin and may be safely delivered to a diagnostic site.

A unique property of SXR microscopy is the capability to study 'living' specimens which are placed in special cells, at normal pressure, achieved due to a rather high transmittance of air (the absorption length is on the order of 1 mm).

On the strength of the resonance nature of radiation absorption by biological samples, the requisite irradiation dose (the criterion for a dose required for observing objects of arbitrary shape: the number of events in the object must exceed the noise in the matrix fivefold) is 5–7 orders of magnitude lower than in the nonresonance interaction, for instance, when using traditional electron or X-ray microscopy [19]. So strong a lowering of the dose as applied to microscopy involving biological objects signifies that a resolution of 50 nm may be obtained even for living specimens. For this resolution, we are somewhere around a dose limit of $\approx 10^5$ Gy admissible for cells. In this case, the sample's temperature will rise by about 25°. With the application of sample freezing, it is possible to safely study organic materials with a resolution of 10 nm and less.

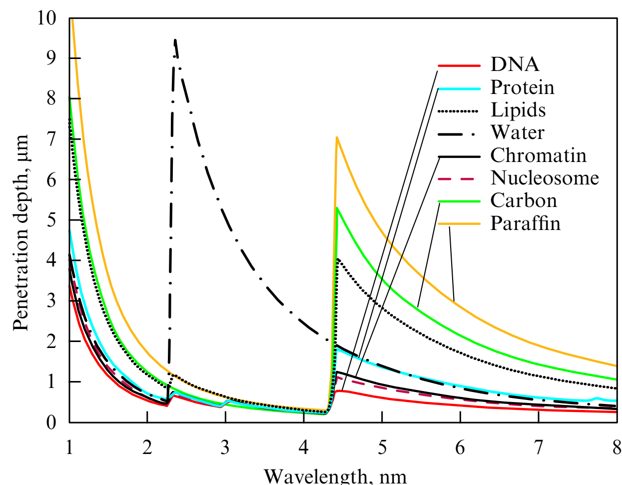

Figure 13. Spectral dependence of the SXR radiation penetration depth, over which the intensity lowers by e times, for different organic compounds and water. The figure was borrowed from Ref. [108].

The existence of X-ray absorption jumps in this region permits revealing and identifying individual chemical elements, for instance, potassium (absorption L-edge at 4.2 nm) and calcium (absorption L-edge at 3.5 nm) by recording images at two wavelengths, below and above the absorption edge of the element selected. Therefore, that which is indeed impossible for conventional electron and X-ray microscopies becomes a reality in the soft X-ray region.

Until recently, most work on SXR microscopy had been conducted using an FZP for a condenser, and an imaging element according to the configuration proposed in Ref. [103]. In Section 2 we discussed the main disadvantages of applying FZPs for these purposes and, in particular, their low efficiency, as well as low numerical and geometrical apertures, with the consequential large depth of focus (DOF $= \lambda/\mathrm{NA}^2 \approx 300$ nm for $\lambda = 3$ nm and NA $= 0.1$) and short focal distance (hundreds of micrometers), which impede studying samples in special cells [104]. All this is a severe limitation on the introduction of soft X-ray microscopy to laboratory practice.

With the development of the synthesis technology of ultrashort-period MISs which may work at the angles of normal incidence in the $\lambda > 2.3$ nm range, an alternative to zone plates appeared for imaging with a high spatial resolution. The simplest projection imaging scheme is the Schwarzschild lens; in the classical version, it consists of two spherical mirrors (convex and concave) with MISs deposited on their surfaces, the MIS reflectivities being optimized for the working wavelength. In this configuration, a two-mirror

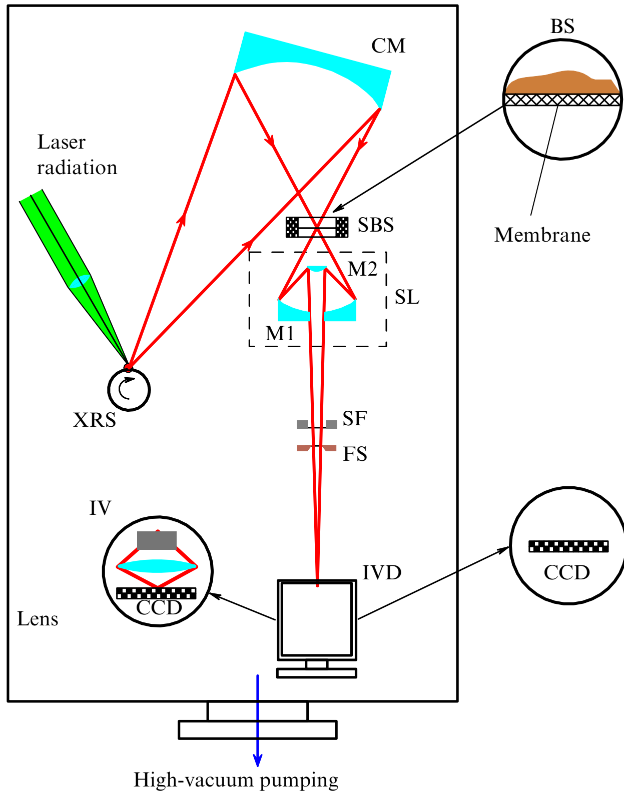

Figure 14. Diagram of a projection X-ray microscope. XRS – X-ray source, CM — collector mirror, SBS — three-axis stage with a biological sample, FS — field stop, BS — biological sample under study, SL — Schwarzschild lens comprising mirrors M1 and M2, SF — spectral filter, IVD — image visualization device, IV — image visualizer, and CCD — optical or X-ray back-illuminated CCD array.

lens permits compensating for fifth-order axial aberrations [105].

Despite the fact that work with X-ray mirror microscopes has been pursued for a rather long time [106–108], a spatial resolution of a fraction of a micrometer attained to date is still appreciably worse than that of FZP-based microscopes. As discussed above, the main reason lies in the absence of fabrication technologies for substrates with the requisite shape accuracy at an RMS < 0.1–0.30 nm level.

Figure 14 displays a schematic of the projection X-ray microscope with a two-mirror lens. The source radiation is focused on the sample under investigation with the aid of a normal-incidence collector mirror with a reflective multilayer coating. The collector aperture is determined from the requirement of matching the field of view to the input angular aperture of the lens and the radiation source size. The sample under study is placed at the lens object plane. Located at the image plane is an image visualization device (IVD) — a detector. Two image visualization systems are considered, depending on the lens resolution. Shown at the left of Fig. 14 is an image visualizer (IV) which comprises a transparent thin plate coated with a thin scintillator layer for X-ray-to-visible radiation conversion. With the aid of a wide-aperture magnifying optical lens, the image on the scintillator is transferred to an optical CCD array where it is recorded, digitized, and fed to a computer in real time. The second image visualization version, which is shown at the right, involves direct recording of the X-ray images with a CCD camera. This version requires an X-ray lens with a magnification of several hundred times.

The image contrast may be improved by obtaining the subtractive pattern of two images simultaneously taken at two wavelengths, at the maximum and minimum of absorption of the element selected. For instance, MISs with different resonance wavelengths (at the carbon absorption peak at a wavelength $\lambda_1 \leqslant 4.37$ nm, and at the absorption minimum $\lambda_2 \geqslant 4.4$ nm) are deposited on the conjugate halves of mirrors M1 and M2. Every chemical element necessitates a lens of its own, and several such lenses may be accommodated in a turret head.

The calculated characteristics of periodic multilayer mirrors optimized for the detection of calcium, potassium, carbon, and nitrogen atoms are collected in Table 4. The wavelength values corresponding to the maximum ($\lambda_{\max}^{\text{abs}}$) and minimum ($\lambda_{\min}^{\text{abs}}$) of the X-ray absorption are given in parentheses. The data are given for both ideal structures (roughness $\sigma = 0$) and a more realistic value of $\sigma = 0.3$ nm. One can see from Table 4 that the substitution of cobalt for chromium results in about a 1.5-fold increase in integral MIS reflectivity. Also given are the admissible departures of MIS period thicknesses from their nominal values (Δd), which correspond to reflectivity peak shifts by a half of the Bragg peak width. The period departures in magnitude amount to a hundredth of a nanometer and less.

From the standpoint of technology, the deposition of such a structure is a highly intricate task in view of the sphericity or asphericity of the substrate surface and the gradient distribution of the period over the surface (at every point of radiation incidence on the surface the Bragg condition must be fulfilled). In the case of a two-mirror lens, the requirements for the accuracy of the period distributions over the surface and with structure depth are even more stringent, because every point on the mirror surface corresponds to a specific point on the surface of the other mirror, and the periods at each point are strictly prescribed. That is, apart from the exact law of period distribution over the surface of each mirror, the absolute value of the period at every surface point must approximate the prescribed value to within 0.1%.

Since the requirements for the spectral transmission band of a mirror microscope are much lower than for an FZP, it is possible to substantially broaden the transmission band and, accordingly, raise the integral reflection coefficients of the mirrors due to an aperiodic layer thickness distribution with depth of the MIS [109]. The broadening of the reflectivity curve also leads to the second positive effect — a lowering of the requirements for the accuracy of MIS deposition. In our opinion, the application of rigorous algorithms for optimizing the composition of aperiodic structures would permit a significant increase in their efficiency and a lowering of the requirements imposed on the accuracy of deposited film thicknesses.

Rigorous calculations of the optical characteristics of a two-mirror Schwarzschild lens formed by spherical mirrors lead to the following conclusion: for a high numerical aperture (NA $\approx 0.3-0.5$) and a large magnification (100–300), even the compensation for fifth-order aberrations is insufficient for obtaining diffraction-limited resolution. To solve this problem, it would suffice to make the shape of one of the lens mirrors aspheric, with the aspheric surface departure from the ideal sphere not exceeding 500 nm.

To estimate the efficiency of recording images with the aid of detectors for different kinds of microscopes, which is

Table 4. Calculated characteristics of periodic multilayer mirrors optimized for the detection of calcium, potassium, carbon, and nitrogen atoms.

λ, nm	MIS	d, nm	$\sigma = 0$				$\sigma = 0.3$ nm			
			R, %	$\Delta\lambda$, nm	$\lambda/\Delta\lambda$	Δd, nm	R, %	$\Delta\lambda$, nm	$\lambda/\Delta\lambda$	Δd, nm
Ca ($\lambda_{max}^{abs} \approx 3.52$ nm, $\lambda_{min}^{abs} \approx 3.60$ nm)										
3.52	Cr/Sc	1.765	30	0.016	220	0.008	12	0.014	250	0.007
3.52	Co/Sc	1.765	36	0.020	176	0.01	15	0.016	220	0.008
K ($\lambda_{max}^{abs} \approx 4.21$ nm, $\lambda_{min}^{abs} \approx 4.27$ nm)										
4.25	Cr/Sc	2.14	36	0.020	212	0.01	13.6	0.019	223	0.01
4.25	Co/Sc	2.14	29	0.030	142	0.015	16	0.026	163	0.013
C ($\lambda_{max}^{abs} \approx 4.33$ nm, $\lambda_{min}^{abs} \approx 4.45$ nm)										
4.33	Co/Sc	2.18	29	0.31	137	0.016	16	0.029	150	0.014
4.45	Co/C	2.23	45	0.34	131	0.017	27.5	0.030	150	0.015
N ($\lambda_{max}^{abs} \approx 2.99$ nm, $\lambda_{min}^{abs} \approx 3.10$ nm)										
2.99	Co/Ti	1.50	30	0.0125	240	0.006	8.5	0.01	300	0.005
3.12	Co/Sc	1.56	56	0.0185	169	0.009	26	0.012	260	0.006

Table 5. Calculated characteristics of laboratory microscopes based on aspheric multilayer optics and Fresnel zone plates.

λ, nm	Microscope type	NA	δx, nm	Ω_c, sr	I	$G = I_{MIS}/I_{FZP}$
2.36	PZP	0.079	18	2.2×10^{-3}	2.6×10^{-8}	1.6×10^{-3}
	PM	0.3	10	3.1×10^{-2}	4.2×10^{-11}	
	CZP	0.079	10	2.2×10^{-3}	9.2×10^{-7}	0.13
	CM	0.079	10	2.2×10^{-3}	1.2×10^{-7}	
	SZP	0.079	20	8.8×10^{-9}	1.1×10^{-13}	0.23
	SM	0.3	18	1.27×10^{-7}	2.5×10^{-14}	
3.14	PZP	0.105	18	2.2×10^{-3}	2.6×10^{-8}	11
	PM	0.3	10	3.1×10^{-2}	2.9×10^{-7}	
	CZP	0.079	10	2.2×10^{-3}	9.2×10^{-7}	3.2
	CM	0.079	10	2.2×10^{-3}	2.9×10^{-6}	
	SZP	0.079	18	8.8×10^{-9}	1.1×10^{-13}	100
	SM	0.3	18	1.27×10^{-7}	1.1×10^{-11}	
4.47	PM	0.3	10	3.1×10^{-2}	1.7×10^{-6}	64

Notation: projection mirror (PM), projection zone plate-based (PZP), contact mirror (CM), contact zone plate-based (CZP), scanning mirror (SM), and scanning zone plate-based (SZP) microscopes; δx — resolution, NA — numerical aperture, Ω_c — solid angle of the source radiation collector, I — detector signal, and G — efficiency ratio between the MIS- and FZP-based microscopes.

defined as the number of photons per pixel of the CCD camera, the detector signal $I_d(\lambda)$ can be written down as

$$I_d(\lambda) = N_{ph}\, I_1 = S\Omega_c \int R_c(\lambda)\, R_{ob}(\lambda)\, d\lambda\,,$$

where N_{ph} is the number of photons incident on the detector, I_1 is the detector current induced by a photon, S is the product of detector responsivity and the emission characteristic of the radiation source per unit solid angle and spectral range expressed in A W^{-1} and W (sr by 1 nm)$^{-1}$, respectively, Ω_c is the solid angle intercepted by the photon collector, and R_c and R_{ob} are parameters of the imaging optical elements, namely the radiation transmission coefficients in the case of FZPs, and the reflectivities of the multilayer mirrors of the collector and the lens in the case of mirror optics. The efficiency of a two-mirror lens is determined by the product of mirror reflectivities.

The estimated results of image recording efficiency for X-ray microscopes based on two FZPs [40] and those based on mirror optics are given in Table 5, which imply that the mirror microscopes are higher in efficiency at working

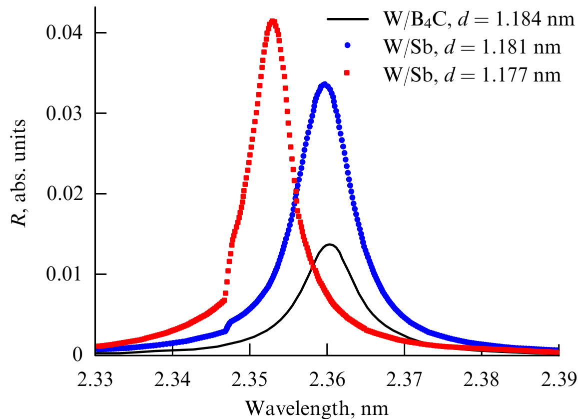

Figure 15. Comparison of the spectral characteristics of W/B_4C and W/Sb MISs in the vicinity of $\lambda = 2.3$ nm. Roughness $\sigma = 0.24$ nm.

wavelengths $\lambda > 3$ nm. This is explained by their greater geometrical and angular apertures, as well as higher peak and integral reflectivities. Furthermore, the mirror microscope efficiencies were calculated for the existing MISs optimized, in the majority of cases, for other tasks. If, for instance, instead of W/B_4C, use is made of a W/Sb MIS, whose fabrication was shown to be technologically feasible earlier [110], then, as shown by calculations (Fig. 15), the mirror microscope efficiency at a wavelength $\lambda = 2.3$ nm will rise by nearly two orders of magnitude and approach the efficiency of the FZP-based microscope. In the contact and scanning microscope operation modes, its efficiency will exceed that of the FZP microscope.

Large mirror diameters permit the first optical element and the sample under study to be substantially moved away from the radiation source by up to several hundred millimeters, which is critically important in the operation with laboratory radiation sources (laser plasma, gas discharge), whose erosion products (material droplets, fast ions and neutral particles, hot electrons) may damage the samples. The large numerical apertures and long focal distances of mirror lenses permit achieving a spatial resolution as high as several nanometers in the 3–10 nm spectral range. Furthermore, because of the high numerical aperture, the depth of focus of the mirror lens may be as short as ≈ 20 nm, making it possible to reconstruct the three-dimensional object image with a resolution of better than 20 nm by translating the object along the axis.

Therefore, the development and application of high-resolution mirror lenses offer new possibilities in soft X-ray microscopy, including the study of 'living' biological objects. This was made possible by the recent breakthrough advancements made in the metrology and fabrication of ultrahigh-precision optical elements and systems with subnanometer-level wave aberrations, as well as in the deposition of high-reflectivity short-period multilayer interference structures with compensated internal strains.

It is pertinent to note that reflection microscopy may be a powerful aid in solving an intricate practical problem — revelation of defects in multilayer mask blanks (multilayer mirrors with requisite barrier layers intended for the subsequent formation of magnified microchip topology on their surface) and defects of masks fabricated for nanolithography at wavelengths of 13.5 and 6.7 nm. The problem resides in the fact that it is required to detect defects down to 30 nm in size. Since a multilayer structure participates in the radiation reflection, the defects may be surface imperfections or bulk defects. Surface defects may by discovered by traditional methods, including light scattering (for a mask blank). However, bulk defects, for instance, local imperfections of the interference structure arising from the presence of clusters ranging from a fraction of a nanometer to tens of nanometers in size on the substrate surface or in the multilayer coating are not necessarily detectable by conventional atomic-force or electron microscopy techniques.

Reflection defect microscopy is a direct technique, since a study is made of the radiation reflection from a mask at the working wavelength under conditions similar to those in a nanolithography tool. An FZP may also be employed for imaging, but mirror optics is the method of choice not only due to reflection efficiency, but also due to the large field of view with the use of aspherical optics. The latter is of critical importance, since in practice the productivity of defectoscopic procedures has to be taken into account because the mask surface area is rather large, reaching ≈ 200 cm^2.

To summarize this section, mention should be made of recent work on the X-ray microscopy of condensed matter with the use of resonance radiation–matter interaction. The heart of this technique is as follows: in the presence of material property anisotropy (for instance, magnetization of the medium or electric polarization), dependence of the medium's absorption coefficient on the radiation polarization appears due to atomic energy level shifts in the vicinity of material absorption edges. To state it in different terms, absorption contrast may be observable in a chemically homogeneous material. In particular, mention should be made of a pioneering study on nanomagnetism, in which the magnetic dichroism effect was utilized to observe the formation of domains in a $(Co_{0.83}Cr_{0.17})_{87}Pt_{13}$ film and reconstruct with a 15-nm spatial resolution the map of magnetic moments and the dynamics of domain walls in relation to the applied magnetic field [20].

Since the effect is general in nature and is inherent in all structured media with anisotropy of optical constants, this method opens up unique possibilities for the study of 'nanoelectromagnetism' due to its nanometer-scale spatial resolution and a relatively high radiation penetrability into a substance.

5.3 X-ray astronomy

One more area in which the employment of precision X-ray optics is of fundamental importance covers astrophysical investigations of the solar corona. Investigations of the Sun are of special interest, because it is the only star which humanity can comprehensively study in real time with the high spatial and temporal resolutions. Apart from the purely scientific character of studying the phenomena and processes occurring in the depths of and on the surface of stars, these investigations have recently acquired enormous practical significance as well, because the processes associated with energy liberation in the solar corona determine the state of the interplanetary medium and, in particular, the circumterrestrial medium. They make the main contribution to the increase in radiation background and define to a large extent the state of the magnetosphere, ionosphere, and upper layers of the terrestrial atmosphere, thereby affecting anthropogenic activity of the mankind. Thus, investigations of the corona are of importance for the study of the solar–terrestrial relationships and forecasting geoeffective events and their

possible consequences. This research area is making rapid strides and is referred to as 'space weather' [111].

SXR and EUV imaging spectroscopy in the line radiation of multiply charged ions is one of the main methods of studying the structure and dynamics of plasma objects in the solar corona. In this case, spatial resolution is the key link to the solution to several basic problems of solar physics, in particular, the problem of solar corona heating, the problem of triggers of solar flares and mass ejections, etc. In the opinion of astrophysicists, the spatial resolution must be maintained at a level of several hundred kilometers, which corresponds to an angular resolution in the range $0.1''$–$0.15''$ [112].

Over the past 20 years, the spatial resolution and sensitivity of X-ray telescopes have been improved manyfold, which was largely due to the employment of normal-incidence X-ray multilayer mirrors. In this connection, it is pertinent to note that the TEREK telescope became the prototype for modern X-ray telescopes: it made the first use of the combination of X-ray multilayer mirrors and high-sensitivity digital sensors based on image-convertor amplifiers and CCD arrays [113]. The TEREK telescope and all subsequent Russian telescopes have been equipped with X-ray multilayer optics developed and fabricated at the IPM of the RAS. In particular, aspherical multilayer mirrors 100 mm in diameter, which were constituent parts of the TESIS telescope made in the framework of the CORONAS-PHOTON project, enabled achieving a spatial resolution close to the size of one CCD array pixel, thus corresponding to an angular resolution of about one arcsecond. Figure 16 exemplifies a solar corona image at a wavelength of 30.4 nm, obtained in the framework of the TESIS experiment in 2009 [114].

Among the solar experiments currently underway, mention should be made of the development of the ultrahigh-resolution ARKA observatory [115] (projected for launch in 2015) aimed at reaching an angular resolution of $0.17''$, which corresponds to ≈ 130 km on the solar surface. Realization of this angular resolution necessitates the fabrication of precision aspherical optics with the lens aperture up to 50 cm in diameter.

Figure 16. Prominence eruption on the eastern solar limb on 23 April 2009: TESIS observations in the 304-Å line of He II. The plasma temperature is about 80 thousand kelvins [114].

One of the key issues in creating an EUV telescope stems from the necessity of suppressing the high-intensity background radiation of the Sun, primarily in the visible spectral region. Similar problems also have to be solved in the development of an EUV nanolithography tool, an X-ray microscope, and the systems of X-ray diagnostics of high-temperature laboratory plasmas. The requirements imposed on spectral filters may vary greatly from application to application. Notably, the filters employed in the telescopes must suppress the radiation of the visible spectral region by 12 orders of magnitude for a sufficiently high transmittance, on the order of tens of percent, at the working wavelength. The filters must be able to withstand mechanical loads (vibration and acoustic loads, especially during the takeoff of the rocket carrier) and endure severe thermal conditions for many years. For all of the aforementioned applications, multilayer cantilever-like filters with apertures up to 180 mm have been developed at the IPM, RAS, either on a supporting mesh with cell sizes ranging from 2 to 20 mm or without support structures at all [116, 117].

5.4 Superhigh soft X-ray fields

The last 10–15 years have seen vigorous research into the interaction of high-intensity femtosecond laser pulses with matter, especially with atomic cluster beams [118]. These investigations are aimed at the basic laws of radiation–matter interaction and the production of photons and elementary particles with energies far greater than the energy of laser photons.

In several papers, for instance in review [119], the mechanisms of radiation–matter interaction (heating and acceleration of electrons and ions, ionization) have been shown to depend strongly on the photon energy and radiation power density. It was shown, in particular, that while the 'field' mechanism — acceleration in the electromagnetic wave field — makes the greatest contribution to the heating of plasma electrons in the visible region, in the near-EUV range (95-nm wavelength) this takes place due to electron collisions. The mechanisms of primary atomic ionization also change. By and large, the efficiency of radiation energy transformation to the energy (heating) of the cluster substance was shown to be high with decreasing radiation wavelength.

Apart from new radiation–matter interaction effects, shortening the wavelength by two orders of magnitude in comparison with the visible range permits — if diffraction-quality optics is available — decreasing the focal spot area by four orders of magnitude and reaching a focal spot intensity of over 10^{21} W cm^{-2} even with the existing FLASH free-electron laser (DESY, Hamburg) [120] (its main radiation characteristics are given in Table 6). In radiation intensity, this is comparable to the capabilities of femtosecond lasers of the optical range, though in a shorter-wavelength domain.

Raising the electron energy to 2.5 GeV, as considered in the NGL-2500 free-electron laser project [121], as well as optimizing the lasing band and the photon energy, will enable increasing the intensity up to $\sim 10^{23}$ W cm^{-2}. The implementation of this experiment will permit observing new electromagnetic radiation–matter interaction effects, because this experiment will combine record high radiation (field) power densities with individual photon energies which are at resonance with atomic transitions.

Table 6. Key parameters of the FLASH (Hamburg, FRG) free-electron laser (FEL) and the projected NGL-2500 (Dubna, RF) FEL (data borrowed from Refs [120, 121].

Parameter	FLASH	NGL-2500
Electron energy, MeV	680	2500
Macropulse duration, ms	0.8	0.8
Number of pulses in a macropulse	7200	8000
Macropulse repetition rate, Hz	10	10
Radiation wavelength, nm	13.5	13.5
Spectral bandwidth, %	2	2
Pulse energy, mJ	1.4	33
Pulse duration, fs	250	250
Peak power, GW	5.6	130
Average radiation power, W	100	2640
At-focus intensity, W cm^{-2}	1.3×10^{21}	3.0×10^{22}

6. Conclusion

We have made a review of the current state-of-the-art of research in the areas of fabrication and applications of a new class of optics, which may be thought of as mature — normal-incidence multilayer optics for the SXR and EUV ranges. Due to the enormous progress of recent years in the deposition technology of multilayer coatings for X-ray mirrors and the fabrication and certification of optical elements and diffraction-quality systems for the SXR and EUV ranges, it has become possible to transfer the wealth of traditional methods of controling light beams (monochromatization, focusing, collimation, imaging, beam splitting, polarizing, phase shifting elements and analyzers, etc.) to the short-wavelength (nanometer-level) range. This has opened up new avenues for condensed matter microscopy and research in biology, astrophysics, and other areas. Mention should be made of the huge potential for employing these optics in nanotechnologies, first and foremost in lithography and nanodiagnostics.

This progress has resulted from extensive research in several related areas of solid-state, surface, thin-film-structure growth physics, physical optics, and some others. It has called for the advancement of perfect technologies for growing multilayer structures and new methods and technologies for fabricating and characterizing optical elements and systems with unprecedented accuracy. In this connection, the role of the Institute for Physics of Microstructures (IPM, RAS) in the development of this research area should be emphasized.

Acknowledgments. This work was supported by the Russian Foundation for Basic Research under grants Nos 09-02-00912, 10-02-00957, 11-02-00597, 11-02-00961, and 11-02-97109-r, and the Federal Task-Oriented Program 'Scientific and Scientific-Pedagogical Personnel of Innovative Russia' in 2009–2013.

References

1. Moore G E *Electronics* **38** 114 (1965); *Proc. IEEE* **86** 82 (1998), reprinted
2. Rosa L G, Liang J *J. Phys. Condens. Matter* **21** 483001 (2009)
3. Pease R F *Microelectron. Eng.* **78–79** 381 (2005); "Charged particle maskless lithography", in *30th Intern. Conf. on Micro & Nano Engineering, 2004*
4. Hirayanagi N et al. *Proc. SPIE* **5037** 504 (2003)
5. Giannuzzi L A, Stevie F A (Eds) *Introduction to Focused Ion Beams: Instrumentation, Theory, Techniques, and Practice* (New York: Springer, 2005)
6. Ginger D S, Zhang H, Mirkin C A *Angew. Chem. Int. Ed.* **43** 30 (2003)
7. Wong A K-K *Resolution Enhancement Techniques in Optical Lithography* (Bellingham, Wash.: SPIE Press, 2001)
8. Drapeau M et al. *Proc. SPIE* **6521** 652109 (2007)
9. ASML, http://www.asml.com/asml/show.do?ctx = 6720& rid = 36951
10. Haran B et al. *IEEE Electron Dev. Meeting Proc.* 625 (2008)
11. Pohl D W, Denk W, Lanz M *Appl. Phys. Lett.* **44** 651 (1984)
12. Naulleau P et al. *J. Vac. Sci. Technol. B* **20** 2829 (2002)
13. Van Dijsseldonk A "Concept of ASML EUV tool — lithographic aspects", in *'NanoCMOS (Pull-Nano)'/'More Moore' Event "Beyond 45 nm Technologies", Belgium, IMEC, 9–10 May 2006*
14. Salashchenko N N, Chkhalo N I *Vestnik Ross. Akad. Nauk* **78** 450 (2008) [*Herald Russ. Acad. Sci.* **78** 279 (2008)]
15. Wagner Ch, Harned N *Nature Photon.* **4** 24 (2010)
16. Dmitrienko V E, Ovchinnikova E N *Kristallografiya* **48** (Suppl. 1) 59 (2003) [*Crystallogr. Rep.* **48** (Suppl. 1) S52 (2003)]
17. Basov N G et al. *Diagnostika Plotnoi Plazmy* (Diagnostics of Dense Plasma) (Ed. N G Basov) (Moscow: Nauka, 1989)
18. Mandel'shtam S L et al. "Izmereniya pri pomoshchi geofizicheskikh raket" ("Measurements using geophysical rockets"), in *Iskusstvennye Sputniki Zemli* (Artificial Earth Satellites) Issue 10 *Issledovanie Rentgenovskogo Izlucheniya Solntsa* (Investigation of X-Ray Solar Radiation) (Moscow: Izd. AN SSSR, 1961) p. 12
19. Kirz J, Jacobsen C, Howells M *Quart. Rev. Biophys.* **28** 33 (1995)
20. Fischer P *Mater. Today* **13** (9) 14 (2010)
21. Oreshko A P, Dmitrienko V E, Ovchinnikova E N *Fundament. Priklad. Mat.* **15** (6) 151 (2009) [*J. Math. Sci.* **172** 859 (2009)]
22. Kulipanov G N, Skrinskii A N *Usp. Fiz. Nauk* **122** 369 (1977) [*Sov. Phys. Usp.* **20** 559 (1977)]
23. Saldin E L, Schneidmiller E A, Yurkov M V *The Physics of Free Electron Lasers* (Berlin: Springer, 2000)
24. Koshelev K N, Banine V E, Salashchenko N N *Usp. Fiz. Nauk* **177** 777 (2007) [*Phys. Usp.* **50** 741 (2007)]
25. Hansson B A M et al. *Microelectron. Eng.* **53** 667 (2000)
26. Attwood D, Halbach K, Kim K-J *Science* **228** 1265 (1985)
27. Lee T N, McLean E A, Elton R C *Phys. Rev. Lett.* **59** 1185 (1987)
28. Andreev S S et al. *Izv. Ross. Akad. Nauk., Ser. Fiz.* **69** 207 (2005)
29. Andreev S S et al. *Nucl. Instrum. Meth. Phys. Res. A* **543** 340 (2005)
30. Henke B L, Gullikson E M, Davis J C *Atom. Data Nucl. Data Tabl.* **54** 181 (1993)
31. The Center for X-Ray Optics: "X-Ray interactions with matter", http://henke.lbl.gov/optical_constants/
32. Vinogradov A V et al. *Zerkal'naya Rentgenovskaya Optika* (Mirror X-ray Optics) (Ed. A V Vinogradov) (Leningrad: Mashinostroenie, 1989)
33. Kirkpatrick P, Baez A V *J. Opt. Soc. Am.* **38** 766 (1948)
34. Wolter H *Ann. Physik* **10** 94 (1952)
35. Mimura H et al. *Appl. Phys. Lett.* **90** 051903 (2007)
36. Arkad'ev V A, Kumakhov M A *Poverkhnost': Fizika, Khimiya, Mekhanika* (10) 25 (1986)
37. Jark W et al. *Appl. Phys. Lett.* **78** 1192 (2001)
38. Snigirev A et al. *Nature* **384** 49 (1996)
39. Schmahl G, Rudolph D (Eds) *X-Ray Microscopy* (Berlin: Springer-Verlag, 1984) [Translated into Russian: *Rentgenovskaya Optika i Mikroskopiya* (Moscow: Mir, 1987)]
40. Chao W et al. *Nature* **435** 1210 (2005)
41. Weiss D, Peuker M, Schneider G *Appl. Phys. Lett.* **72** 1805 (1998)

42. Schneider G, Rehbein S, Werner S, in *Modern Developments in X-Ray and Neutron Optics* (Eds A Erko et al.) (New York: Springer Science + Business Media, 2008) p. 137
43. Rehbein S et al. *Phys. Rev. Lett.* **103** 110801 (2009)
44. Spiller E *AIP Conf. Proc.* **75** 124 (1981)
45. Barbee T W *Opt. Eng.* **25** 898 (1986)
46. Andreev S S et al. *Centr. Eur. J. Phys.* **1** 191 (2003)
47. Gaponov S V et al. *Opt. Commun.* **38** 7 (1981)
48. Platonov Yu Y, Gomez L, Broadway D *Proc. SPIE* **4782** 152 (2002)
49. Andreev S S et al. *J. Synchrotron Rad.* **10** 358 (2003)
50. Vainer Yu A et al. *Zh. Eksp. Teor. Fiz.* **130** 401 (2006) [*JETP* **103** 346 (2006)]
51. Shamov E A, Prokhorov K A, Salashchenko N N *Poverkhnost': Rentgen., Sinkhrotron. Neitronnye Issled.* (9) 60 (1996)
52. Salashchenko N N, Shamov E A *Opt. Commun.* **134** 7 (1997)
53. Sakano K, Yamamoto M *Proc. SPIE* **3767** 238 (1999)
54. Kuhlmann T et al. *Appl. Opt.* **41** 2048 (2002)
55. Gullikson E M, in *Intern. Conf. on Physics of X-Ray Multilayer Structures, PXRMS'06, Sapporo, Japan, March 12–16, 2006*; http://www.esrf.eu/files/Conferences/pxrms06/booklet.pdf
56. Schäfers F et al. *Appl. Opt.* **38** 4074 (1999)
57. Gaponov S V et al. *Zh. Tekh. Fiz.* **56** 708 (1986)
58. Andreev A V, Michette A G, Renwick A *J. Mod. Opt.* **35** 1667 (1988)
59. Holý V et al. *Phys. Rev. B* **47** 15896 (1993)
60. Schmahl G, Rudolph D (Eds) *X-Ray Microscopy* (Berlin: Springer-Verlag, 1984) [Translated into Russian: *Rentgenovskaya Optika i Mikroskopiya* (Moscow: Mir, 1987) p. 305]
61. Chkhalo N I et al., in *X-Ray Microscopy IV. XRM'93. Proc. of the 4th Intern. Conf., Chernogolovka, Russia, Sept. 20–24, 1993* (Eds V V Aristov, A I Erko) (Chernogolovka: Bogorodskii Pechatnik, 1994) p. 586
62. Vainer Yu A et al. *Izv. Ross. Akad. Nauk Ser. Fiz.* **75** 65 (2011) [*Bull. Russ. Acad. Sci. Phys.* **75** 61 (2011)]
63. Stearns D G *J. Appl. Phys.* **65** 491 (1989)
64. Savage D E et al. *J. Appl. Phys.* **69** 1411 (1991)
65. Renner O et al. *Rev. Sci. Instrum.* **63** 1478 (1992)
66. Andreev A V et al. *Pis'ma Zh. Eksp. Teor. Fiz.* **66** 219 (1997) [*JETP Lett.* **66** 236 (1997)]
67. Akhsakhalyan A D et al. *Thin Solid Films* **203** 317 (1991)
68. Andreev S S et al. *Nucl. Instrum. Meth. Phys. Res. A* **603** 80 (2009)
69. Andreev S S et al. *Zh. Tekh. Fiz.* **80** (8) 93 (2010) [*Tech. Phys.* **55** 1168 (2010)]
70. Parratt L G *Phys. Rev.* **95** 359 (1954)
71. Michaelsen C et al. *Opt. Lett.* **26** 792 (2001)
72. Zuev S Yu et al. *Poverkhnost': Rentgen., Sinkhrotron. Neitronnye Issled.* (1) 32 (2002)
73. André J-M et al. *X-Ray Spectrometry* **34** 203 (2005)
74. Malacara D (Ed.) *Optical Shop Testing* 2nd ed. (New York: Wiley, 1992)
75. Zygo Corporation, http://www.zygo.com
76. Salashchenko N N, Toropov M N, Chkhalo N I *Izv. Ross. Akad. Nauk Ser. Fiz.* **74** 62 (2010) [*Bull. Russ. Acad. Sci. Phys.* **74** 53 (2010)]
77. Chkhalo N I et al., in *Lithography* (Ed. M Wang) (Vukovar, Croatia: INTECH, 2010) p. 656; http://sciyo.com/articles/show/title/manufacturing-and-investigating-objective-lens-for-ultrahigh-resolution-lithography-facilities
78. Barysheva M M et al. *Izv. Ross. Akad. Nauk Ser. Fiz.* **75** 71 (2011) [*Bull. Russ. Acad. Sci. Phys.* **75** 67 (2011)]
79. Linnik V P *Izv. Akad. Nauk SSSR* **1** 210 (1933) [*C.R. Acad. Sci. USSR* **1** 208 (1933)]
80. Sommargren G E *Laser Focus World* **32** (8) 61 (1996)
81. Naulleau P P et al. *Appl. Opt.* **38** 7252 (1999)
82. Otaki K et al. *J. Vac. Sci. Technol. B* **20** 2449 (2002)
83. Chkhalo N I et al. *Proc. SPIE* **7025** 702507 (2008)
84. Chkhalo N I et al. *Rev. Sci. Instrum.* **79** 033107 (2008)
85. Klyuenkov E B et al. *Ross. Nanotekhnol.* **3** (9–10) 116 (2008) [*Nanotechnol. Russ.* **3** 602 (2008)]
86. Puryaev D T *Metody Kontrolya Opticheskikh Asfericheskikh Poverkhnostei* (Control Methods for Aspheric Optical Surfaces) (Moscow: Mashinostroenie, 1976) p. 13
87. Kurashima Y et al. *Microelectron. Eng.* **85** 1193 (2008)
88. Keller A, Facsko S, Möller W *J. Phys. Condens. Matter* **21** 495305 (2009)
89. Ziegler E *Nucl. Instrum. Meth. Phys. Res. A* **616** 188 (2010)
90. Chkhalo N I et al. *Nucl. Instrum. Meth. Phys. Res. A* **359** 155 (1995)
91. Zuev S Yu et al. *Izv. Ross. Akad. Nauk Ser. Fiz.* **75** 57 (2011) [*Bull. Russ. Acad. Sci. Phys.* **75** 53 (2011)]
92. Barysheva M M et al., in *Nanofizika i Nanoelektronika. Trudy XV Mezhdunarodnogo Simpoziuma* (Nanophysics and Nanoelectronics. Proc. XVth Intern. Symp.), *14–18 March 2011, Nizhny Novgorod* Vol. 1 (N. Novgorod: IFM RAN, 2011) p. 85
93. Dinger U et al. *Proc. SPIE* **4146** 35 (2000)
94. Andreev S S et al. *Poverkhnost': Rentgen., Sinkhrotron. Neitronnye Issled.* (2) 45 (2005)
95. Zuev S Yu et al. *Izv. Ross. Akad. Nauk Ser. Fiz.* **75** 61 (2011) [*Bull. Russ. Acad. Sci. Phys.* **75** 57 (2011)]
96. Wood O et al. *Proc. SPIE* **7271** 727104 (2009)
97. Tawarayama K et al. *Jpn. J. Appl. Phys.* **48** 06FA02 (2009)
98. Gower M ''Photolithography microsteppers'', http://www.electroiq.com/articles/mlw/print/volume-13/issue-1/featured/photolithography-microsteppers.html
99. Volgunov D G et al. *Izv. Ross. Akad. Nauk Ser. Fiz.* **75** 54 (2011) [*Bull. Russ. Acad. Sci. Phys.* **75** 49 (2011)]
100. Zuev S Yu et al. *Poverkhnost': Rentgen., Sinkhrotron. i Neitronnye Issled.* (6) 10 (2011) [*J. Surf. Investigat. X-Ray, Synchr. Neutron Tech.* **5** 517 (2011)]
101. Tsarfati T et al. *Thin Solid Films* **518** 1365 (2009)
102. Artyukov I A et al. *Kvantovaya Elektron.* **34** 691 (2004) [*Quantum Electron.* **34** 691 (2004)]
103. Niemann B, Rudolph D, Schmahl G *Appl. Opt.* **15** 1883 (1976)
104. Parkinson D Y et al. *J. Struct. Biol.* **162** 380 (2008)
105. Hoover R B et al. *Proc. SPIE* **984** 234 (1988)
106. Lovas I et al. *Proc. SPIE* **316** 90 (1981)
107. Tanaka K A et al. *Proc. SPIE* **1140** 502 (1989)
108. Artyukov I A et al. *Kvantovaya Elektron.* **22** 951 (1995) [*Quantum Electron.* **25** 919 (1995)]
109. Kozhevnikov I V, Bukreeva I N, Ziegler E *Nucl. Instrum. Meth. Phys. Res. A* **460** 424 (2001)
110. Salashchenko N N, Platonov Yu Ya, Zuev S Yu *Nucl. Instrum. Meth. Phys. Res. A* **359** 114 (1995)
111. Kuzin S V, Bogachev S A *Voprosy Elektromekhaniki. Trudy NPP VNIIEM* **111** (4) 51 (2009)
112. Urnov A M et al. *Pis'ma Astron. Zh.* **33** 446 (2007) [*Astron. Lett.* **33** 396 (2007)]
113. Zhitnik I A et al. *Trudy Fiz. Inst. Akad. Nauk* **195** 3 (1989)
114. Shestov S V et al. *Pis'ma Astron. Zh.* **36** 46 (2010) [*Astron. Lett.* **36** 44 (2010)]
115. Kuzin S V et al. *Izv. Ross. Akad. Nauk Ser. Fiz.* **75** 91 (2011) [*Bull. Russ. Acad. Sci. Phys.* **75** 87 (2011)]
116. Bibishkin M S et al. *Proc. SPIE* **7025** 702502 (2008)
117. Volodin B A et al. *Izv. Ross. Akad. Nauk Ser. Fiz.* **74** 53 (2010) [*Bull. Russ. Acad. Sci. Phys.* **74** 46 (2010)]
118. Ditmire T et al. *Nature* **386** 54 (1997)
119. Makarov G N *Usp. Fiz. Nauk* **179** 487 (2009) [*Phys. Usp.* **52** 461 (2009)]
120. Saldin E, Report FEEL09 (August 2009)
121. Anchutkin V S et al., in *Nanofizika i Nanoelektronika. Trudy XIV Mezhdunarodnogo Simpoziuma* (Nanophysics and Nanoelectronics. Proc. XIVth Intern. Symp.), *15–19 March 2010, Nizhny Novgorod* Vol. 1 (N. Novgorod: IFM RAN, 2011) p. 209
122. Bibishkin M S et al. *Izv. Ross. Akad. Nauk Ser. Fiz.* **69** 199 (2005)
123. Artyukov I A et al. *Proc. SPIE* **5919** 94 (2005)
124. Montcalm C et al. *Proc. SPIE* **3331** 42 (1998)
125. Bajt S et al. *Proc. SPIE* **4506** 65 (2001)
126. Zuev S Yu et al. *Izv. Ross. Akad. Nauk Ser. Fiz.* **74** 58 (2010) [*Bull. Russ. Acad. Sci. Phys.* **74** 50 (2010)]]